Optical properties of massive anisotropic tilted Dirac systems

M. A. Mojarro [1], R. Carrillo-Bastos [1,*], and Jesús A. Maytorena [2]

[1]*Facultad de Ciencias, Universidad Autónoma de Baja California, Apartado Postal 1880, 22800 Ensenada, Baja California, México*
[2]*Centro de Nanociencias y Nanotecnología, Universidad Nacional Autónoma de México, Apartado Postal 2681,*
22800 Ensenada, Baja California, México

We explore the effect of valley-contrasting gaps in the optical response of two-dimensional anisotropic tilted Dirac systems. We study the spectrum of intraband and interband transitions through the joint density of states (JDOS), the optical conductivity tensor, and the Drude spectral weight. The energy bands present an indirect gap in each valley with a reduced magnitude with respect to the nominal gap of the untilted system. Thus, a new possibility opens for the position of the Fermi level (an "indirect zone") and for the momentum space available for allowed transitions. The JDOS near each gap displays a set of three van Hove singularities which are in contrast to the case of gapped graphene (an absorption edge only) or 8-*Pmmn* borophene (two interband critical points due the tilt). For the Fermi level lying within the gap the JDOS shows the usual linear dependence on frequency, while when lying above an indirect zone it looks similar to the borophene case. These spectral characteristics in each valley determine the prominent structure of the optical conductivity. The longitudinal conductivity illustrates the strong anisotropy of the optical response. Similarly, the Drude weight is anisotropic and shows regions of nonlinear dependence on the Fermi level. The breaking of valley symmetry leads to a finite Hall response and associated optical properties. The anomalous and valley Hall conductivities present graphenelike behavior with characteristic modifications due to the indirect zones. Almost perfect circular dichroism and valley polarization can be achieved by tuning the exciting frequency with an appropriate Fermi level position. We also calculate the spectra of optical opacity and polarization rotation, which can reach magnitudes of tenths of radians in some cases. The spectral features of the calculated response properties are signatures of the simultaneous presence of tilt and mass, and suggest optical ways to determine the formation of different gaps in such class of Dirac systems like 8-*Pmmn* borophene, quinoid-type graphene, organic conductor α-(BEDT-TTF)$_2$I$_3$, or some transition-metal dichalcogenides.

I. INTRODUCTION

Relativistic effects are ubiquitous in two-dimensional materials, and light-matter interaction has become a powerful tool to test its intriguing consequences. From the spatial imaging of the spin Hall effect in two-dimensional electron gasses [1] to the distinctive optical response in graphene [2] and the quantized Faraday and Kerr rotations in topological insulators [3,4], optical techniques have not only served as a probe of nonconventional behavior of these materials but also as a way to extract parameter values for effective models [5,6]. Furthermore, optical properties can be very sensitive to broken symmetries present in the studied system [7–9]. For example, the rotation of the polarization plane after passing through a medium, known as the Faraday effect, can serve as an indicator of the breaking of either time-reversal symmetry (TRS) or inversion symmetry; Even for the thinnest samples [10], like graphene [11] and the surface of topological insulators [12], the Faraday angle can reach several degrees. Similarly, the polar Kerr effect has as a necessary condition the breaking of the TRS. Since both effects are directly related with the ac

conductivity, they offer a contact-free manner to measure the electronic transport properties of materials [7].

When materials display a relativisticlike linear spectrum they are called Dirac materials [13]. Most of these materials present an isotropic spectrum in momentum space [14], a symmetric Dirac cone. Nevertheless, it has been recently found that some of them present anisotropic linear spectra, i.e., tilted anisotropic Dirac cones; such as the case for 8-*Pmmn* borophene [15–18], quinod-type graphene [19], the organic conductor α-(BEDT-TTF)$_2$I$_3$ [20–23], 1T' monolayer transition metal dichalcogenides [24,25] and partially hydrogenated graphene [26]. In general, the presence of a cone tilt does lead to qualitatively different behavior compared with the untilted system [27]; in particular, when interacting with light it gives raise to different optical and electronic properties. Sadhukhan and Agarwal [28] found anisotropic plasmon dispersion, and Sarí *et al.* a unique intervalley damping effect for magnetoplasmons [29,30]. Likewise, it has been found that the dc conductivity becomes strongly anisotropic between the parallel and perpendicular direction to the tilt [31], while the frequency dependent optical conductivity acquires a non-monotonic behavior with energy that allows to extract the tilting parameter from optical measurements [32–34]. Being semimetals, these materials have zero energy gap, but a gap

*Corresponding author: ramoncarrillo@uabc.edu.mx

can be generated artificially [35–42]. In general, the emergence of a gap can be related with the breaking of a symmetry. For example, in graphene the otherwise semimetallic behavior, can be changed by breaking inversion symmetry [43], which results in the opening of a band gap and the consequent valley Hall effect. Perhaps, the most noticeable example of this, is the quantum Hall effect in graphene [44], which is obtained by placing graphene in a perpendicular magnetic field. Haldane [45] showed with an example that the presence of a magnetic field was not necessary condition, but the breaking of TRS. An alternative way, to generate a Hall conductivity by breaking TRS without a magnetic field, is the spin-texture proposed by Hill *et al.* [46]. In Hill's model, the localized spins of ad-atoms doping one of the sublattices of graphene arrange themselves creating a spin configuration with tilted spins, which can be described by an effective tight-binding Hamiltonian with valley dependent gaps. The latter effect drastically modifies the density of states (DOS) profile, as well as the optical longitudinal and anomalous Hall conductivities. Such a mechanism has been recently invoked in an experiment which show evidence of spinglass formation in hydrogenated graphene [47]. Aside of the spin-textured graphene, there are other Dirac systems with valley asymmetric gap, like gated silicene [48], α-(BEDT-TTF)$_2$I$_3$ with magnetic modulations [49], and the modified Haldane model [50]. Although the optical properties of tilted anisotropic Dirac systems have been subject of intense research [51–61], up to our knowledge the effect of valley dependent gaps [25,62–67] in the optical properties of a tilted anisotropic Dirac system, has not been reported yet. In this paper we present such a study. In this respect, we note that *ab initio* calculations suggest that a band opening in 8-*Pmmn* borophene is possible by hydrogenation and that its direct or indirect nature could be controlled by strain [62]. On the experimental side, the massive fermion state of the mentioned Dirac system α-(BEDT-TTF)$_2$I$_3$ has been recently confirmed [23], making of it a good candidate material for our study. Moreover, excitation with circularly polarized light combined with different on-site potential on underlying sublattices could produce a net valley-dependent mass, as was discussed in Ref. [65].

The outline of the paper is the following. In Sec. II we present the Dirac-like Hamiltonian and its energy band structure, identifying the effect of tilting and anisotropy, the nonuniform gapped valleys, and Fermi contours. In Sec. III we study the optical transitions near the gaps. We first study the joint density of states to identify critical points, which will determine the prominent spectral features of the optical response (Sec. III A). The electrical conductivity tensor, due to intra and interband transitions, is calculated in Sec. III B within the Kubo formalism. The Drude weight is discussed in Sec. III C. In Sec. IV we present optical properties of our system. The anisotropy of the response, circular dichroism spectrum and valley polarization are studied in Sec. IV A. The anomalous and valley Hall conductivities are obtained in Sec. IV B, and compared to the model of gapped graphene with broken valley symmetry developed by Hill *et al.* [46]. Spectra of transmission as a function of angles of incidence and polarization for several positions of the Fermi level is considered in Sec. IV C. In Sec. IV D we calculate spectra of Kerr and Faraday rotation. Finally, we present our conclusions

in Sec. V. There are two appendices with expressions of Fermi contours and related quantities, and of the Fresnel amplitudes describing the problem of refraction of a 2D system between two dielectrics.

II. THE HAMILTONIAN: ANISOTROPY, TILT, AND VALLEY-CONTRASTING GAPS

We consider a 2D anisotropic tilted Dirac system with momentum-space Hamiltonian

$$H^\xi(\mathbf{k}) = \xi(\hbar v_t k_y \mathbb{I} + \hbar v_x k_x \sigma_x + \xi \hbar v_y k_y \sigma_y) + \Delta^\xi \sigma_z, \quad (1)$$

where σ_i are the Pauli matrices acting on the pseudospin space, $\mathbb{I}$ is the identity matrix and $\xi = \pm$ (or K, K') is a valley index; the electron wave vector $\mathbf{k} = (k_x, k_y)$ is measured from the nominal Dirac point in each valley. In addition to the broken particle-hole symmetry (PHS), the model include a valley-contrasting mass, $\Delta^+ \neq \Delta^-$, which breaks the time-reversal symmetry (TRS). For $\Delta^\xi = 0$ the Hamiltonian describes the low lying excitations of two tilted Dirac cones like in some 2D graphene-type materials or some organic conductors subjected to pressure and uniaxial strain [19,29,31,32,53]. The Hamiltonian of graphene is recovered by additionally taking $v_t = 0$ and $v_x = v_y = v_F$. While 8-*Pmmn* borophene Hamiltonian is recovered by taking $v_x = 0.86\, v_F$, $v_y = 0.69\, v_F$, $v_t = 0.32\, v_F$, with $v_F = 10^6$ m/s, and $\Delta^\xi = 0$ [53]. However, first-principles calculations predict the band gap opening in 8-*Pmmn* borophene by hydrogenation [62]. By combining hydrogen adsorption sites, coverage, and mechanical strain the possibility of transition from a direct to indirect band gap is observed. Another material which presents characteristics as those of the Hamiltonian Eq. (1), is the organic conductor α-(BEDT-TTF)$_2$I$_3$. This is a 2D system with a pair of tilted and anisotropic Dirac cones, as was experimentally verified by several types of measurements [22]. Furthermore, the experimental confirmation of massive Dirac fermions was recently reported [23]. Some two-dimensional transition metal dichalcogenides present also tilted Dirac bands around Dirac points with indirect gaps openend by spin-orbit interaction and controllable with electric fields and strain [24,25]. The study presented below about the modification of the spectrum of interband transitions in the vicinity of an indirect gap might be useful for that systems.

The Hamiltonian Eq. (1) has recently been considered to study a valley Seebeck effect [65]. The valley-dependent gap is explained by combining two contributions, a valley-dependent mass photoinduced by circularly polarized light and different on-site energies on the two sublattices, although no particular considerations on the effects due to the indirect nature of the gaps is presented.

The energy-momentum dispersion relation corresponding to the Hamiltonian in Eq. (1) is

$$\varepsilon_\lambda^\xi(k_x, k_y) = \xi \alpha_t k_y + \lambda \sqrt{\alpha_x^2 k_x^2 + \alpha_y^2 k_y^2 + (\Delta^\xi)^2}, \quad (2)$$

where $\alpha_i = \hbar v_i$ ($i = x, y, t, F$), and the index $\lambda = \pm$ defines the energy branch and the helicity of the states in the conduction ($\lambda = +$) and the valence ($\lambda = -$) bands in each valley.

The bands Eq. (2) have critical points at $\mathbf{k}^* = (0, -\xi\lambda Q^\xi)$, where $Q^\xi = (|\Delta^\xi|/\alpha_y)(\gamma/\sqrt{1-\gamma^2})$, yielding a minimum
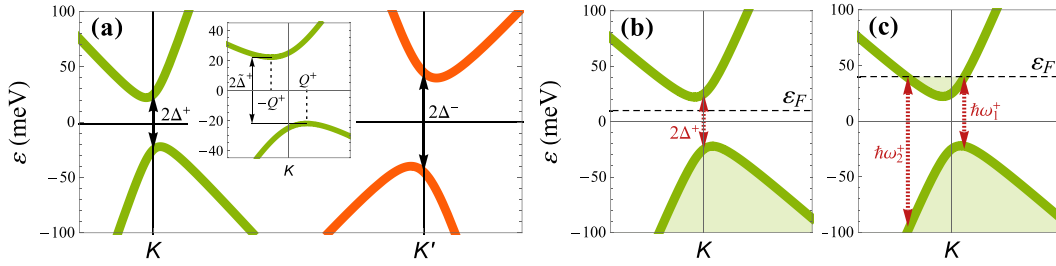
FIG. 1. (a) Energy spectrum of an anisotropic tilted Dirac system with valley symmetry breaking [Eq. (2)]. The smallest vertical energy differences $2\Delta^\xi$ for each valley are shown ($\Delta^+ = 25$ meV, $\Delta^- = 45$ meV). The indirect nature of the gaps is illustrated in the inset (K valley). The points $\mathbf{k}^* = (0, \mp Q^+)$ correspond to the minimum and maximum of the branches. (b) Fermi level lying within a gap, $\varepsilon_F < \tilde{\Delta}^+$. (c) Fermi level lying above a gap, $\varepsilon_F > \Delta^+$ with allowed interband transitions. The energies $\hbar\omega_1^+$, $\hbar\omega_2^+$ give the minimum and maximum energies needed for interband transition.

of ε_+^ξ at $(0, -\xi Q^\xi)$ and a maximum of ε_-^ξ at $(0, \xi Q^\xi)$ [see the inset in Fig. 1(a)]; we have introduced the tilting parameter $\gamma = v_t/v_y$ ($0 \leqslant \gamma < 1$, nonovertilted cones). Note then that $\min\{\varepsilon_+^\xi(\mathbf{k})\} - \max\{\varepsilon_-^\xi(\mathbf{k})\} = \varepsilon_+^\xi(0, -\xi Q^\xi) - \varepsilon_-^\xi(0, \xi Q^\xi) = 2|\Delta^\xi|\sqrt{1-\gamma^2}$ is smaller than the smallest vertical energy difference $\min\{\varepsilon_+^\xi(\mathbf{k}) - \varepsilon_-^\xi(\mathbf{k})\} = \varepsilon_+^\xi(0) - \varepsilon_-^\xi(0) = 2|\Delta^\xi|$. Thus, as a consequence of the simultaneous presence of tilting (γ) and mass (Δ^ξ) there is an indirect band gap at each valley around the nominal Dirac point; see Fig. 1. This implies for example that a Fermi level in the gap means now $|\varepsilon_F| < \min\{|\tilde{\Delta}^+|, |\tilde{\Delta}^-|\}$, where $\tilde{\Delta}^\xi = \Delta^\xi\sqrt{1-\gamma^2} < \Delta^\xi$. Indeed, for each valley the following scenarios are now possible according to the position of the Fermi level: (i) $|\varepsilon_F| > |\Delta^\xi|$ (Fermi level above the nominal direct gap), (ii) $|\tilde{\Delta}^\xi| < |\varepsilon_F| < |\Delta^\xi|$ (Fermi level in an "indirect gap" region), (iii) $|\varepsilon_F| < |\tilde{\Delta}^\xi|$ (Fermi level in the absolute gap); see Fig. 1. This will cause additional structure in the optical response in contrast to the untilted case ($\gamma = 0$). Now the Fermi contours, defined by the curves $C_\lambda^\xi = \{\mathbf{k} | \varepsilon_\lambda^\xi(\mathbf{k}) = \varepsilon_F\}$, are the displaced ellipses $(1 - \gamma^2)\alpha_x^2(k_{\lambda,x}^\xi)^2 + (1 - \gamma^2)^2\alpha_y^2(k_{\lambda,y}^\xi + \xi\lambda Q^\xi |\varepsilon_F|/|\tilde{\Delta}^\xi|)^2 = \varepsilon_F^2 - (\tilde{\Delta}^\xi)^2$ centered at $(0, -\xi\lambda Q^\xi |\varepsilon_F|/|\tilde{\Delta}^\xi|)$ with the major semiaxis along the k_y-direction. Note that when the Fermi level lies in an indirect zone $|\tilde{\Delta}^\xi| < |\varepsilon_F| < |\Delta^\xi|$ the ellipse resides completely in the region $k_y < 0$ ($k_y > 0$) for $\lambda = +$ ($\lambda = -$) [see Fig. 2(d)] which modifies significantly the momentum space available for interband transitions, with respect to that of the case $|\varepsilon_F| > |\Delta^\xi|$. The roots of equation $\varepsilon_\lambda^\xi(\mathbf{k}) = \varepsilon_F$ are displayed in Appendix A.

III. OPTICAL TRANSITIONS NEAR AN INDIRECT GAP

As a previous step to the calculation of the optical conductivity tensor and to understand the spectral features of the optical response of the system, we first consider the joint density of states (JDOS). In the following we adopt the generic notation of a two-band model and write the Hamiltonian and its spectrum as $H^\xi(\mathbf{k}) = \varepsilon_0^\xi(\mathbf{k})\mathbb{I} + \boldsymbol{\sigma} \cdot \mathbf{d}^\xi(\mathbf{k})$ and $\varepsilon_\lambda^\xi(\mathbf{k}) = \varepsilon_0^\xi(\mathbf{k}) + \lambda d^\xi(\mathbf{k})$, where $\varepsilon_0^\xi(\mathbf{k}) = \xi\alpha_t k_y$, $\mathbf{d}^\xi(\mathbf{k}) = \xi\alpha_x k_x\hat{\mathbf{x}} + \alpha_y k_y\hat{\mathbf{y}} + \Delta^\xi\hat{\mathbf{z}}$, and $d^\xi(\mathbf{k}) = |\mathbf{d}^\xi(\mathbf{k})|$. In polar coordinates we write $\mathbf{k} = k\cos\theta\hat{\mathbf{x}} + k\sin\theta\hat{\mathbf{y}}$ and

$$\varepsilon_\lambda^\xi(k, \theta) = \xi\alpha_F kh(\theta) + \lambda\sqrt{\alpha_F^2 k^2 g^2(\theta) + (\Delta^\xi)^2}, \quad (3)$$

in terms of the adimensional quantities $h(\theta) = (\alpha_t/\alpha_F)\sin\theta$, which characterize the tilting dependence, and $g^2(\theta) = (\alpha_x^2/\alpha_F^2)\cos^2\theta + (\alpha_y^2/\alpha_F^2)\sin^2\theta$ which accounts for the anisotropic dispersion. The roots of equation $\varepsilon_\lambda^\xi(k(\theta), \theta) = \varepsilon_F$ are denoted by $k_{\lambda,F}^\xi(\theta)$ when $|\varepsilon_F| > |\Delta^\xi|$ [Fig. 2(b)], and by $q_{\lambda,F}^{\xi,\pm}(\theta)$ if $|\tilde{\Delta}^\xi| < |\varepsilon_F| < |\Delta^\xi|$ [Fig. 2(d)]; see Appendix A for expressions of these roots. In the later case, the $\pm$ sign refers to the two arcs [in green (red) for the sign $-(+)$ in Fig. 2(d)] forming the ellipse which lies completely in the $k_y < 0$ (C_+^+, C_-^-) or $k_y > 0$ (C_+^+, C_-^-) half space; the roots $q_{\lambda,F}^{\xi,\pm}(\theta)$ are defined only in the sector $|\theta - 3\pi/2| < \theta_\xi^*$ if $\xi\lambda = +$, or for $|\theta - \pi/2| < \theta_\xi^*$ if $\xi\lambda = -$, where $\tan\theta_\xi^* = (v_y/v_x)\sqrt{[\varepsilon_F^2 - (\tilde{\Delta}^\xi)^2]/[(\Delta^\xi)^2 - \varepsilon_F^2]}$.

A. Joint density of states

The number of pair of states in conduction (unoccupied) and valence (occupied) bands separated by a given energy $\hbar\omega$ is given by $\mathcal{J}(\omega) = \sum_{\xi=\pm}\mathcal{J}^{(\xi)}(\omega)$ with

$$\mathcal{J}^{(\xi)}(\omega) = g_s \int' \frac{d^2k}{(2\pi)^2}\delta(\varepsilon_+^\xi(\mathbf{k}) - \varepsilon_-^\xi(\mathbf{k}) - \hbar\omega), \quad (4)$$

where $g_s = 2$ is the spin degeneracy and the prime on the integral indicates a range of integration restricted to that region of $\mathbf{k}$ space for which $\varepsilon_-^\xi(\mathbf{k}) < \varepsilon_F < \varepsilon_+^\xi(\mathbf{k})$. However, the δ function restricts the integration to points lying on the resonance curve $\mathcal{C}_r^\xi(\omega) = \{(k_x, k_y) | 2d^\xi(k_x, k_y) = \hbar\omega\}$. Thus, the integral Eq. (4) has to be carried out over those portions of the curve $\mathcal{C}_r^\xi(\omega)$ lying within the $\mathbf{k}$-region for which the previous inequality (Pauli blocking) is satisfied. The curve $\mathcal{C}_r^\xi(\omega)$ is the ellipse centered at the origin $\alpha_x^2 k_{r,x}^2 + \alpha_y^2 k_{r,y}^2 = (\hbar\omega/2)^2 - (\Delta^\xi)^2$, defined only for $\hbar\omega \geqslant 2|\Delta^\xi|$, or in polar coordinates $2\alpha_F k_r(\theta)g(\theta) = \sqrt{(\hbar\omega)^2 - (2\Delta^\xi)^2}$ [Figs. 2(b) and 2(d)]. Indeed, for a given frequency Eq. (4) can be written as a line integral of $(\hbar v_\mathbf{k})^{-1} = |\boldsymbol{\nabla}_\mathbf{k}[2d^\xi(\mathbf{k})]|^{-1}$ over those portions of the curve of constant interband energy $\mathcal{C}_r^\xi(\omega)$ lying in the regions imposed by Pauli blocking. Peaks in the JDOS will appear due to electronic excitations involving states with allowed wave vectors on $\mathcal{C}_r^\xi(\omega)$ such that $v_\mathbf{k}$ takes extreme values. The energy difference $2d^\xi(k, \theta)$ between the conduction and valence bands at the Fermi lines $k_{\lambda,F}^\xi(\theta)$ and $q_{\lambda,F}^{\xi,\pm}(\theta)$ will be denoted by $\hbar\omega_\lambda^\xi(\theta)$ and $\hbar v_\lambda^{\xi,\pm}(\theta)$, respectively (see Appendix A). For $\gamma = 0$ these energies reduce to the same value
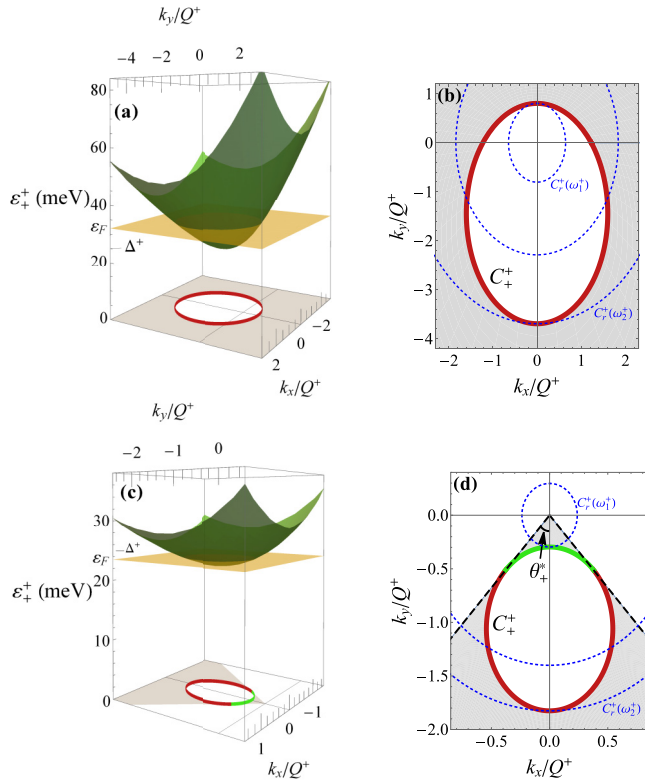
FIG. 2. Conduction energy band $\varepsilon_+^+(\mathbf{k})$ at the K valley. The gap parameter is $\Delta^+ = 25$ meV. At the Fermi level, the contour line $C_+^+ = \{\mathbf{k}|\varepsilon_+^+(\mathbf{k}) = \varepsilon_F\}$ is an ellipse displaced along the k_y axis by $Q^+(\varepsilon_F/\tilde{\Delta}^+)$, with $\tilde{\Delta}^+ = \Delta^+\sqrt{1 - \gamma^2}$. (a) $\varepsilon_F > \Delta^+$, with $\varepsilon_F = 32$ meV. (b) Fermi contour $k_{+,F}^+(\theta)$ displayed in (a). The gray shaded region indicates the momentum space available for optical transitions, such that $\varepsilon_-^+(\mathbf{k}) < \varepsilon_F < \varepsilon_+^+(\mathbf{k})$. (c) Fermi level in the indirect zone $\tilde{\Delta}^+ < \varepsilon_F < \Delta^+$, with $\varepsilon_F = 23.5$ meV. (d) Fermi contour showed in (c). It is defined by the two arcs $q_{+,F}^{+,-}(\theta)$ (green) and $q_{+,F}^{+,+}(\theta)$ (red) in the half-space $k_y < 0$, within the sector $|\theta - 3\pi/2| < \theta_+^*$. As a consequence, the corresponding $\mathbf{k}$-region for interband transitions is strongly reduced. In (b) and (d) the resonance curve $\mathcal{C}_r^+(\omega) = \{\mathbf{k}|\varepsilon_+^+(\mathbf{k}) - \varepsilon_-^+(\mathbf{k}) = \hbar\omega\}$ is presented for several frequencies (dotted lines). It is an ellipse centered at the origin, defined for $\hbar\omega > 2\Delta^+$. At the critical frequencies ω_1^+, ω_2^+ [see Fig. 1(b)] $\mathcal{C}_r^+$ is tangential to the Fermi lines. At a given frequency, only the arcs of $\mathcal{C}_r^+$ lying in the shaded region contribute to the optical response.

$2|\varepsilon_F|$, which is the threshold (above the gap) for interband transitions in gapped graphene. Given the tilt of the bands around each valley, it is verified that $\hbar\omega_-^\xi(\theta) = \hbar\omega_+^\xi(\theta \pm \pi)$ and $\hbar v_-^{\xi,\pm}(\theta) = \hbar v_+^{\xi,\pm}(\theta \pm \pi)$. The minimum and the maximum of these energy differences take place at $\theta = \pi/2$ or $3\pi/2$, and they are all given by the same functions of the Fermi level,

$$\hbar\omega_1^\xi(\varepsilon_F) = \frac{2}{1 - \gamma^2}\left(|\varepsilon_F| - \gamma\sqrt{\varepsilon_F^2 - (\tilde{\Delta}^\xi)^2}\right), \quad (5)$$

$$\hbar\omega_2^\xi(\varepsilon_F) = \frac{2}{1 - \gamma^2}\left(|\varepsilon_F| + \gamma\sqrt{\varepsilon_F^2 - (\tilde{\Delta}^\xi)^2}\right), \quad (6)$$

such that $\min_\theta\{\hbar\omega_\pm^\xi(\theta)\} = \min_\theta\{\hbar v_\pm^{\xi,-}(\theta)\} = \hbar\omega_1^\xi < 2|\varepsilon_F|$ and $\max_\theta\{\hbar\omega_\pm^\xi(\theta)\} = \max_\theta\{\hbar v_\pm^{\xi,+}(\theta)\} = \hbar\omega_2^\xi > 2|\varepsilon_F|$. As

was mentioned above, $\hbar\omega_1^\xi(\gamma = 0) = \hbar\omega_2^\xi(\gamma = 0) = 2|\varepsilon_F|$. Equations (5) and (6) suggest optical measurements of $\omega_{1/2}^\xi$ to determine the tilting and gap parameters. Indeed, we can recover them through the expressions $\gamma = \sqrt{1 - (4|\varepsilon_F|/\varepsilon_s)}$ and $[\Delta^\xi(\omega_1^\xi, \omega_2^\xi)]^2 = |\varepsilon_F|[\hbar\omega_1^\xi\hbar\omega_2^\xi - \varepsilon_s|\varepsilon_F|]/(\varepsilon_s - 4|\varepsilon_F|)$, where $\varepsilon_s = \hbar\omega_1^+ + \hbar\omega_2^+ = \hbar\omega_1^- + \hbar\omega_2^-$.

Integral Eq. (4) looks different according to the position of the Fermi level:

(i) $|\varepsilon_F| > |\Delta^\xi|$

In this case, Pauli blocking and energy conservation restricts to $k_r(\theta, \omega) \geqslant k_{\lambda,F}^\xi(\theta)$, which leads to the result

$$\mathcal{J}^{(\xi)}(\omega) = g_s\frac{\hbar\omega}{8\pi\alpha_F^2}\frac{1}{2\pi}\int_0^{2\pi}\frac{d\theta}{g^2(\theta)}\Theta[\omega - \omega_\lambda^\xi(\theta)], \quad (7)$$

where the sign $\lambda = +\ (-)$ is used when $\varepsilon_F > 0\ (<0)$; $\Theta(x)$ is the Heaviside unit step function. In Fig. 3(c) the JDOS $\mathcal{J}^{(+)}(\omega)$ as calculated from Eq. (7) is shown. For photon energies $\hbar\omega_1^\xi < \hbar\omega < \hbar\omega_2^\xi$, the angular region in momentum space available for vertical transitions is no longer $0 \leqslant \theta \leqslant 2\pi$ as in the untilted case, but a reduced region with a boundary determined by $\hbar\omega_+^+(\theta)$ (top panel). This is in contrast to the well known onset $\Theta(\hbar\omega - 2\varepsilon_F)$ for interband transitions between bands with electron-hole symmetry. The characteristic and unique threshold $2\varepsilon_F$ observed in the optical response of graphene [68] becomes a region bounded by the critical energies $\hbar\omega_1^+$ and $\hbar\omega_2^+$, where the frequency dependence is no longer lineal (bottom panel), because of the tilt of the bands. The JDOS vanishes for $\hbar\omega < \hbar\omega_1^\xi$. When $\hbar\omega > \hbar\omega_2^\xi$ the whole angular region $0 \leqslant \theta \leqslant 2\pi$ contributes, giving the result $\mathcal{J}^{(\xi)}(\omega > \omega_2^\xi) = (g_s/8\pi)(\hbar\omega/\alpha_x\alpha_y)$, which is independent of the tilting parameter α_t and shows the usual linear ω-dependence of Dirac systems. Globally, Fig. 3(c) displays qualitatively a similar behavior as that reported by Verma *et al.* for borophene [32].

(ii) $|\tilde{\Delta}^\xi| < |\varepsilon_F| < |\Delta^\xi|$

Now the momentum space available for direct transitions is restricted to $k_r(\theta, \omega) \geqslant q_{\lambda,F}^{\xi,+}(\theta)$ or $0 \leqslant k_r(\theta, \omega) \leqslant q_{\lambda,F}^{\xi,-}(\theta)$ [Fig. 2(d)] and the JDOS for the valley ξ reads as

$$\mathcal{J}^{(\xi)}(\omega) = g_s\frac{\hbar\omega}{8\pi\alpha_F^2}\frac{1}{2\pi}\Theta(\hbar\omega - 2|\Delta^\xi|)$$
$$\times \int_{\theta_0 - \theta_\xi^*}^{\theta_0 + \theta_\xi^*}\frac{d\theta}{g^2(\theta)}\{\Theta[v_\lambda^{\xi,-}(\theta) - \omega]$$
$$+ \Theta[\omega - v_\lambda^{\xi,+}(\theta)]\}, \quad (8)$$

where $\theta_0 = 3\pi/2\ (\pi/2)$ when $\xi\lambda = +\ (-)$. We also find that $\mathcal{J}^{(\xi)}(2|\Delta^\xi| \leqslant \hbar\omega \leqslant \hbar\omega_1^\xi) = \mathcal{J}^{(\xi)}(\hbar\omega > \hbar\omega_2^\xi) = (g_s/8\pi)(\hbar\omega/\alpha_x\alpha_y)[1 - (2\beta_\xi/\pi)]/2$, where $\tan\beta_\xi = \sqrt{[(\Delta^\xi)^2 - \varepsilon_F^2]/[\varepsilon_F^2 - (\tilde{\Delta}^\xi)^2]}$. The JDOS Eq. (8) for the valley $\xi = +$ is shown in Fig. 3(b). The spectrum displays van Hove singularities at $2\Delta^+$, $\hbar\omega_1^+$, and $\hbar\omega_2^+$, and a reduced overall size in comparison to the cases $|\varepsilon_F| < |\tilde{\Delta}^\xi|$ or $|\varepsilon_F| > |\tilde{\Delta}^\xi|$. Now a linear behavior as a function of photon energy $\hbar\omega$ appears, with a lower slope, in two separated domains only. Moreover, the number of interband transitions is strongly diminished between $\hbar\omega_1^+$ and $\hbar\omega_2^+$ because the angular space available for transitions is considerably
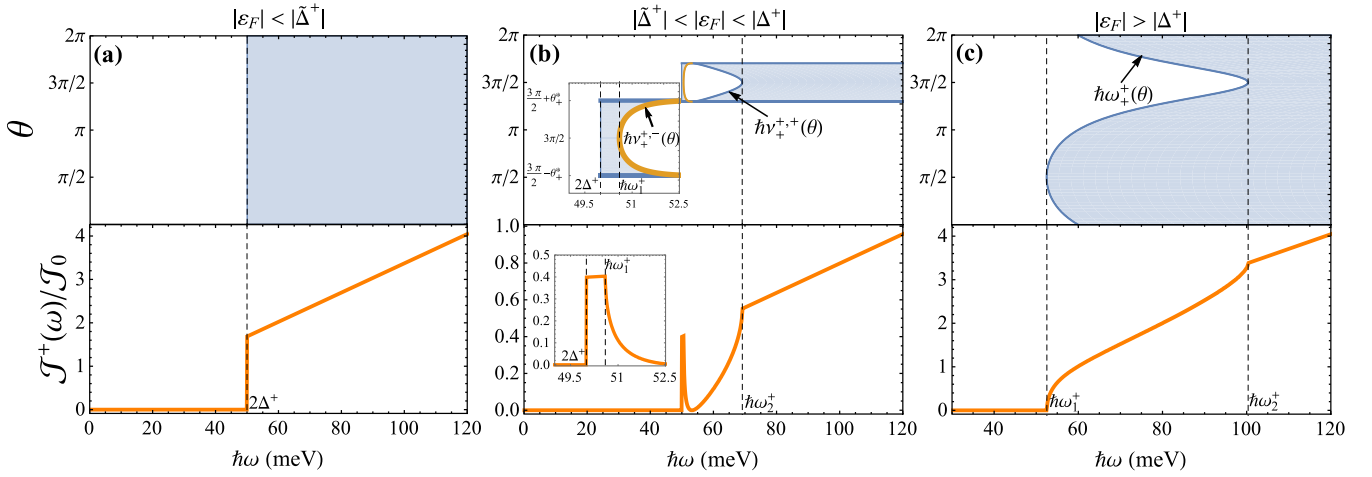
FIG. 3. Joint density of states for transitions at the K valley: (a) $|\varepsilon_F| < |\tilde{\Delta}^+|$, (b) $|\tilde{\Delta}^+| < |\varepsilon_F| < |\Delta^+|$, and (c) $|\varepsilon_F| > |\Delta^+|$. We take $\Delta^+ = 25$ meV and $\mathcal{J}_0 = (g_s/8\pi)(2|\Delta^+|/\alpha_F^2)$.

smaller, as is illustrated in the top panel of Fig. 3(b). The insets show how the contributing angular region narrows for $\omega_1^+ < \omega < \nu_+^{+,-}(\theta)$ or $\nu_+^{+,+}(\theta) < \omega < \omega_2^+$, while the whole sector $|\theta - 3\pi/2| < \theta_+^*$ contributes when $2\Delta^+ \leqslant \hbar\omega \leqslant \hbar\omega_1^+$ or $\hbar\omega > \hbar\omega_2^+$. The appearance of three critical energies instead of one (for $|\varepsilon_F| < |\tilde{\Delta}^\xi|$) or two (for $|\varepsilon_F| > |\Delta^\xi|$) constitutes an optical signature of the indirect gap.

(iii) $|\varepsilon_F| < |\tilde{\Delta}^\xi|$

For the Fermi level within the gap the JDOS becomes

$$\mathcal{J}^{(\xi)}(\omega) = (g_s/8\pi)(\hbar\omega/\alpha_x\alpha_y)\Theta(\hbar\omega - 2|\Delta^\xi|). \quad (9)$$

Besides the reduction of the absolute gap ($|\tilde{\Delta}^\xi| < |\Delta^\xi|$), we note that this result is independent of the tilting parameter. The JDOS looks very similar to that corresponding to gapped graphene but now it involves the geometric mean $\sqrt{v_x v_y}$, instead of velocity v_F, due to the anisotropy of the energy dispersion; see Fig. 3(a).

All these results are used to evaluate the frequency dependence of the total JDOS $\sum_\xi \mathcal{J}^{(\xi)}(\omega; \varepsilon_F)$ for a continuous variation of the Fermi level. Figure 4 illustrates well the appearance of onsets and how the lines defined by the critical frequencies evolve and shape the spectrum of JDOS when a gap is open. In Fig. 4(a) we show the result for borophene ($\Delta^+ = \Delta^- = 0$), where the corresponding

critical energies $\hbar\omega_{1,2}(\varepsilon_F)$ are also indicated. The case with only one gap, $\Delta^+ \neq 0$, $\Delta^- = 0$, is shown in Fig. 4(b). The contribution $\mathcal{J}^{(-)}$ behaves as for borophene, with critical frequencies $\hbar\omega_{1,2}^- = 2\varepsilon_F/(1 \pm \gamma)$. However, for transitions near the gapped valley, the spectrum of the contribution $\mathcal{J}^{(+)}$ displays the threshold at $2\Delta^+$ [Eq. (9)], the borders defined by critical frequencies $\hbar\omega_{1,2}^+$ with a nonlinear dependence on ε_F [Eqs. (5) and (6)], and an indirect zone where the joint density is strongly suppressed. Figure 4(c) displays the case with valley-contrasting gaps $|\Delta^-| > |\Delta^+|$.

B. Optical conductivity tensor

Within the framework of the linear response theory, we find that the conductivity tensor $\sigma_{ij}(\omega) = \sum_\xi \sigma_{ij}^{(\xi)}(\omega)$, which determines the electrical current induced in the system by an external homogeneous electric field of frequency ω, has the form

$$\text{Re}\,\sigma_{ii}^{(\xi)}(\omega) = D_{ii}^{(\xi)}\delta(\omega) + \text{Re}\,\sigma_{ii}^{(\xi),\text{inter}}(\omega), \quad (10)$$

$$\text{Im}\,\sigma_{ii}^{(\xi)}(\omega) = \text{Im}\,\sigma_{ii}^{(\xi),\text{intra}}(\omega) + \text{Im}\,\sigma_{ii}^{(\xi),\text{inter}}(\omega), \quad (11)$$

$$\sigma_{xy}^{(\xi)}(\omega) = -\sigma_{yx}^{(\xi)}(\omega) = \sigma_{xy}^{(\xi),\text{inter}}(\omega), \quad (12)$$
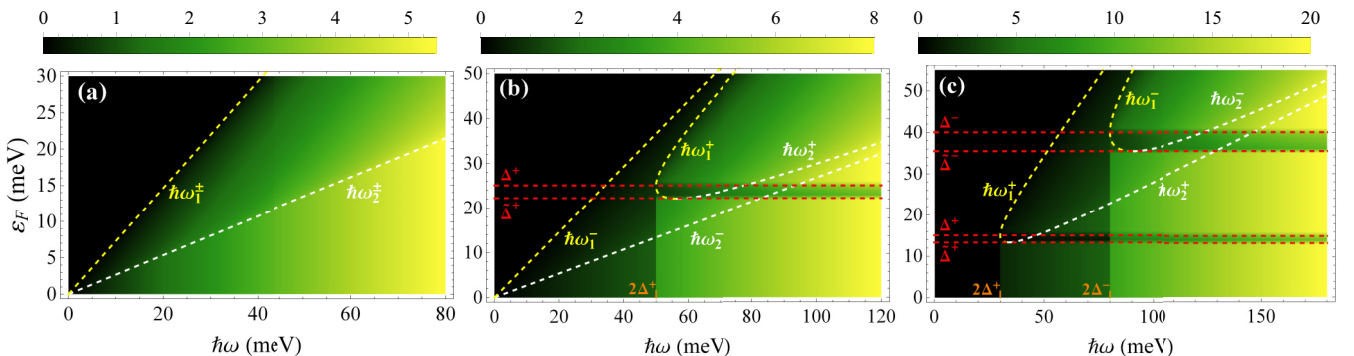

FIG. 4. Total joint density of states $\mathcal{J}(\omega; \varepsilon_F)/\mathcal{J}_0$ considering; (a) $\Delta^+ = \Delta^- = 0$, (b) $\Delta^+ = 25$ meV and $\Delta^- = 0$, and (c) $\Delta^+ = 15$ meV and $\Delta^- = 40$ meV. In panels (b) and (c) we take $\mathcal{J}_0$ as in Fig. 3. In (a) we use $\Delta^+ = 25$ meV in $\mathcal{J}_0$.
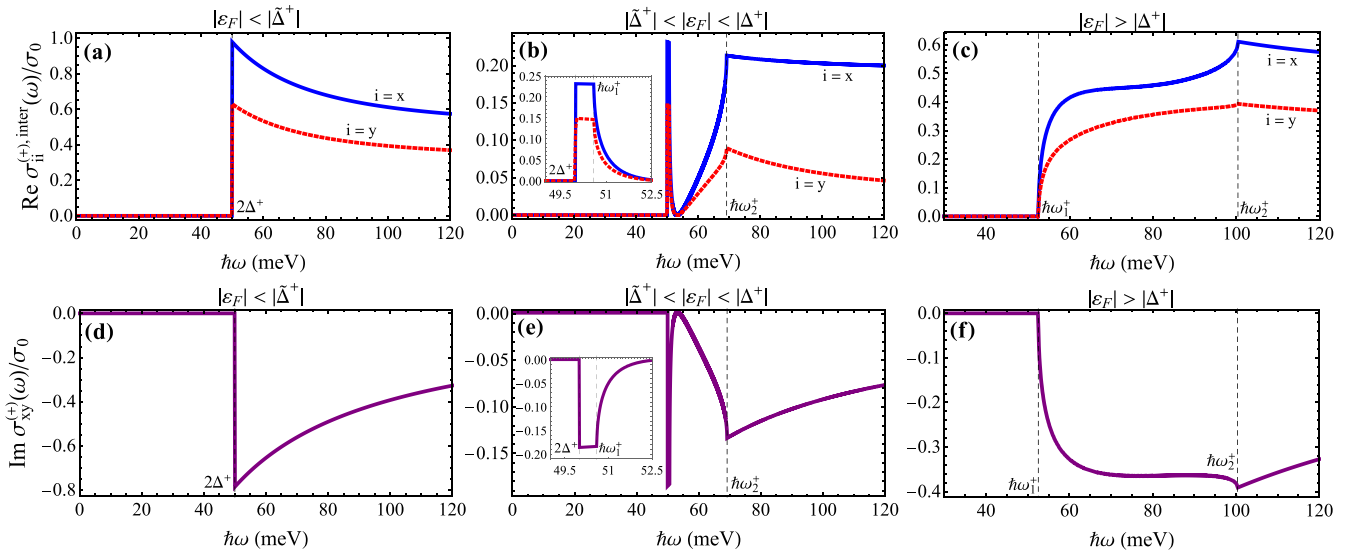
FIG. 5. Dissipative components of the interband conductivity at the K valley, for $|\varepsilon_F| < |\tilde{\Delta}^+|$ (a, d), $|\tilde{\Delta}^+| < |\varepsilon_F| < |\Delta^+|$ (b, e), $|\varepsilon_F| > |\Delta^+|$ (c, f). We take $\Delta^+ = 25$ meV.

where the label intra (inter) refers to contributions due to intraband (interband) transitions. According to the Kubo formula, these are obtained from (at zero temperature)

$$\sigma_{ii}^{(\xi),\mathrm{intra}}(\omega) = ig_s \frac{\sigma_0}{4\pi\hbar\omega} \sum_\lambda \int d^2k \big[V_{\lambda,i}^\xi(\mathbf{k})\big]^2 \delta\big[\varepsilon_\lambda^\xi(\mathbf{k}) - \varepsilon_F\big],$$

$$(13)$$

$$\mathrm{Re}\,\sigma_{ij}^{(\xi),\mathrm{inter}}(\omega) = g_s \frac{\sigma_0}{4\hbar\omega} \int{}' d^2k \frac{S_{ij}^\xi(\mathbf{k})}{[d^\xi(\mathbf{k})]^2} \delta[\hbar\omega - 2d^\xi(\mathbf{k})],$$

$$(14)$$

$$\mathrm{Im}\,\sigma_{ij}^{(\xi),\mathrm{inter}}(\omega) = g_s \frac{\sigma_0}{4\pi\hbar\omega} \mathcal{P} \int{}' d^2k$$
$$\times \frac{S_{ij}^\xi(\mathbf{k})}{[d^\xi(\mathbf{k})]^3} \frac{(\hbar\omega)^2}{(\hbar\omega)^2 - [2d^\xi(\mathbf{k})]^2},\quad (15)$$

$$\mathrm{Re}\,\sigma_{xy}^{(\xi),\mathrm{inter}}(\omega) = g_s \frac{\sigma_0}{2\pi} \mathcal{P} \int{}' d^2k \frac{T_{xy}^\xi(\mathbf{k})}{d^\xi(\mathbf{k})} \frac{1}{(\hbar\omega)^2 - [2d^\xi(\mathbf{k})]^2},$$

$$(16)$$

$$\mathrm{Im}\,\sigma_{xy}^{(\xi),\mathrm{inter}}(\omega) = -g_s \frac{\sigma_0}{8} \int{}' d^2k \frac{T_{xy}^\xi(\mathbf{k})}{[d^\xi(\mathbf{k})]^2} \delta[\hbar\omega - 2d^\xi(\mathbf{k})],$$

$$(17)$$

where $\sigma_0 = 2e^2/h$, $\mathcal{P}$ means Principal Value integral, $V_{\lambda,i}^\xi(\mathbf{k}) = \frac{\partial \varepsilon_0^\xi(\mathbf{k})}{\partial k_i} + \frac{\lambda}{d^\xi} \mathbf{d}^\xi \cdot \frac{\partial \mathbf{d}^\xi}{\partial k_i}$, $S_{ij}^\xi(\mathbf{k}) = (\mathbf{d}^\xi \times \frac{\partial \mathbf{d}^\xi}{\partial k_i}) \cdot (\mathbf{d}^\xi \times \frac{\partial \mathbf{d}^\xi}{\partial k_j})$, and $T_{xy}^\xi(\mathbf{k}) = \mathbf{d}^\xi \cdot (\frac{\partial \mathbf{d}^\xi}{\partial k_x} \times \frac{\partial \mathbf{d}^\xi}{\partial k_y})$. The prime indicates integration over domains which depend on the position of the Fermi energy according to the condition $\varepsilon_-^\xi(\mathbf{k}) < \varepsilon_F < \varepsilon_+^\xi(\mathbf{k})$. We have included in Eq. (10) the Drude weight [69] $D_{ii}^{(\xi)} = \pi \lim_{\omega\to0}[\omega\,\mathrm{Im}\,\sigma_{ii}^{(\xi)}(\omega)] = \pi \lim_{\omega\to0}[\omega\,\mathrm{Im}\,\sigma_{ii}^{(\xi),\mathrm{intra}}(\omega)]$. When the Fermi level lies in the gap, the intraband conductivity is null, only transitions

from the valence into the conduction band contribute. We will work within the infinite band limit.

Figure 5 shows the dissipative components of the optical conductivity tensor for several positions of the Fermi level in the valley $\xi = +$. In accordance to the spectral behavior of JDOS, these spectra show interband critical points and a characteristica reduction of the response when the Fermi level lies in the indirect zone. In contrast to graphene and borophene there is a finite transverse response $\propto \Delta^\xi$. However, the result $\sigma_{xx}^\xi(\omega) \neq \sigma_{yy}^\xi(\omega)$ reveals the anisotropic character of the optical response of the system.

For $|\varepsilon_F| < |\tilde{\Delta}^\xi|$ [Figs. 5(a) and 5(d)] we obtain

$$\mathrm{Re}\,\sigma_{ii}^{(\xi),\mathrm{inter}}(\omega) = g_s \frac{\sigma_0\pi}{16}\left[1 + \left(\frac{2\Delta^\xi}{\hbar\omega}\right)^2\right]$$
$$\times \frac{v_i}{v_x}\frac{v_i}{v_y} \Theta(\hbar\omega - 2|\Delta^\xi|),\quad (18)$$

$$\mathrm{Im}\,\sigma_{xy}^{(\xi),\mathrm{inter}}(\omega) = -\xi g_s \sigma_0 \pi \frac{\Delta^\xi}{4\hbar\omega} \Theta(\hbar\omega - 2|\Delta^\xi|).\quad (19)$$

For the diagonal components it is verified that $v_y^2\,\mathrm{Re}\,\sigma_{xx}^{(\xi),\mathrm{inter}}(\omega) = v_x^2\,\mathrm{Re}\,\sigma_{yy}^{(\xi),\mathrm{inter}}(\omega)$, while the Hall component is independent of v_x, v_y, and v_t. These results look very similar to those of gapped graphene, but with the additional anisotropy factor $v_i^2/v_x v_y \neq 1$ in the diagonal elements.

When $|\varepsilon_F| > |\Delta^\xi|$ [Figs. 5(c) and 5(f)],

$$\mathrm{Re}\,\sigma_{ii}^{(\xi),\mathrm{inter}}(\omega) = g_s \frac{\sigma_0}{16}\left\{\frac{\alpha_x^2}{\alpha_F^2}\frac{\alpha_y^2}{\alpha_F^2}\left[1 - \left(\frac{2\Delta^\xi}{\hbar\omega}\right)^2\right]\right.$$
$$\times \int_0^{2\pi} d\theta \frac{(\delta_{ix}\sin^2\theta + \delta_{iy}\cos^2\theta)}{g^4(\theta)}$$
$$\times \Theta\big[\omega - \omega_\lambda^\xi(\theta)\big]$$
$$\left.+ \frac{\alpha_i^2}{\alpha_F^2}\left(\frac{2\Delta^\xi}{\hbar\omega}\right)^2 \int_0^{2\pi} \frac{d\theta}{g^2(\theta)} \Theta\big[\omega - \omega_\lambda^\xi(\theta)\big]\right\},$$

$$(20)$$

$$\text{Im}\,\sigma_{xy}^{(\xi),\text{inter}}(\omega) = -\xi g_s \sigma_0 \pi \frac{\Delta^\xi}{4\hbar\omega} \frac{\alpha_x}{\alpha_F} \frac{\alpha_y}{\alpha_F} \frac{1}{2\pi}$$

$$\times \int_0^{2\pi} \frac{d\theta}{g^2(\theta)} \Theta\big[\omega - \omega_\lambda^\xi(\theta)\big], \quad (21)$$

where $\lambda = +\ (-)$ if $\varepsilon_F > 0\,(<0)$. We find that $\text{Re}\,\sigma_{ii}^{(\xi),\text{inter}}(\omega < \omega_1^+) = 0$ and

$$\text{Re}\,\sigma_{ii}^{(\xi),\text{inter}}(\omega > \omega_2^+) = g_s \frac{\sigma_0 \pi}{16}\left[1 + \left(\frac{2\Delta^\xi}{\hbar\omega}\right)^2\right]\frac{v_i}{v_x}\frac{v_i}{v_y}. \quad (22)$$

In contrast to the result for borophene ($\Delta^\xi = 0$), Eq. (22) shows a dependence on frequency; only for high enough frequency the universal result $\text{Re}[\sigma_{xx}^{\text{inter}}(\omega > \omega_2^+)] \times \text{Re}[\sigma_{yy}^{\text{inter}}(\omega > \omega_2^+)] = (e^2/4\hbar)^2$ reported by Verma *et al.* [32] can be recovered. However, between ω_1^+ and ω_2^+ Eq. (20) gives a frequency dependence very similar to that of borophene, although with slightly different critical frequencies. Similarly, $\text{Im}\,\sigma_{xy}^{(\xi),\text{inter}}(\omega < \omega_1^+) = 0$ and

$$\text{Im}\,\sigma_{xy}^{(\xi),\text{inter}}(\omega > \omega_2^+) = -\xi g_s \sigma_0 \pi \frac{\Delta^\xi}{4\hbar\omega}. \quad (23)$$

Again, this result is very close to that of gapped graphene for the ξ valley $\text{Im}\,\sigma_{xy}^{gr}(\omega) = -\xi g_s \sigma_0 \pi (\Delta^\xi/4\hbar\omega)\Theta(\hbar\omega - 2\max\{|\varepsilon_F|, |\Delta^\xi|\})$.

Distinctly different behavior occurs when the Fermi level is located within the indirect zone $|\tilde\Delta^\xi| < |\varepsilon_F| < |\Delta^\xi|$ [Figs. 5(b) and 5(e)] because of the strong reduction of the momentum space available for optical transitions, as was discussed about the JDOS. In this narrow window for the Fermi energy we have

$$\text{Re}\,\sigma_{ii}^{(\xi),\text{inter}}(\omega) = g_s \frac{\sigma_0}{16}\,\Theta(\hbar\omega - 2|\Delta^\xi|)$$

$$\times \left(\frac{\alpha_x^2}{\alpha_F^2}\frac{\alpha_y^2}{\alpha_F^2}\left[1 - \left(\frac{2\Delta^\xi}{\hbar\omega}\right)^2\right]\right.$$

$$\times \int_{\theta_0 - \theta_\xi^*}^{\theta_0 + \theta_\xi^*} d\theta\,\frac{\delta_{ix}\sin^2\theta + \delta_{iy}\cos^2\theta}{g^4(\theta)}$$

$$\times \big\{\Theta\big[\nu_\lambda^{\xi,-}(\theta) - \omega\big] + \Theta\big[\omega - \nu_\lambda^{\xi,+}(\theta)\big]\big\}$$

$$+ \frac{\alpha_i^2}{\alpha_F^2}\left(\frac{2\Delta^\xi}{\hbar\omega}\right)^2 \int_{\theta_0 - \theta_\xi^*}^{\theta_0 + \theta_\xi^*} \frac{d\theta}{g^2(\theta)}$$

$$\times \big\{\Theta\big[\nu_\lambda^{\xi,-}(\theta) - \omega\big] + \Theta\big[\omega - \nu_\lambda^{\xi,+}(\theta)\big]\big\}\bigg), \quad (24)$$

$$\text{Im}\,\sigma_{xy}^{(\xi),\text{inter}}(\omega) = -\xi g_s \sigma_0 \pi\,\Theta(\hbar\omega - 2|\Delta^\xi|)\frac{\Delta^\xi}{4\hbar\omega}\frac{\alpha_x}{\alpha_F}\frac{\alpha_y}{\alpha_F}\frac{1}{2\pi}$$

$$\times \int_{\theta_0 - \theta_\xi^*}^{\theta_0 + \theta_\xi^*} \frac{d\theta}{g^2(\theta)} \big\{\Theta\big[\nu_\lambda^{\xi,-}(\theta) - \omega\big]$$

$$+ \Theta\big[\omega - \nu_\lambda^{\xi,+}(\theta)\big]\big\}. \quad (25)$$

As was mentioned above, the spectral features associated to three critical frequencies in the optical response serve as a fingerprint of the simultaneous presence of tilting and mass in the band structure of a 2D Dirac system at low energies. From

Eqs. (18)–(25), it is verified that for $|\Delta^+| = |\Delta^-|$, $\text{Re}\,\sigma_{ii}^{(+)} = \text{Re}\,\sigma_{ii}^{(-)}$, while for $\Delta^+ = \pm\Delta^-$, $\text{Im}\,\sigma_{xy}^{(+)} = \mp\text{Im}\,\sigma_{xy}^{(-)}$.

Now, we comment on the total response function $\sigma_{ij}(\omega) = \sum_\xi \sigma_{ij}^{(\xi)}(\omega)$. In contrast to pristine or (uniformly) gapped graphene, where the conductivity tensor is diagonal and isotropic with an absorption edge defined by $2|\Delta^\xi|$ or $2|\varepsilon_F|$, in our system we have two pairs of tilted cones with different gaps in each valley. It is verified that $\sigma_{xy}(\omega) = 0$ when $\Delta^+ = \Delta^-$, because of the recovery of the time-reversal symmetry. Correspondingly, the inversion symmetry is broken, which anticipates a valley sensitive response.

The three distinct possibilities for the position of the chemical potential, and the corresponding spectral characteristics of the optical conductivity of each valley, open a number of scenarios for the total response. In the following we list the distinctive cases:

(1) A closed gap in one valley and an open gap in the other. For instance, $\Delta^+ \neq 0$, $\Delta^- = 0$:

    (i) $|\varepsilon_F| < |\tilde\Delta^+|$,

    (ii) $|\tilde\Delta^+| < \varepsilon_F < |\Delta^+|$,

    (iii) $|\varepsilon_F| > |\Delta^+|$.

(2) ε_F within the absolute gap, $|\varepsilon_F| < \min\{|\tilde\Delta^+|, |\tilde\Delta^-|\}$.

(3) Nonoverlapping indirect zones, $|\tilde\Delta^+| < |\Delta^+| < |\tilde\Delta^-| < |\Delta^-|$.

    (i) ε_F at the indirect zone at K but within the gap at K', $|\tilde\Delta^+| < |\varepsilon_F| < |\Delta^+| < |\tilde\Delta^-|$.

    (ii) ε_F above the direct zone at K, but in the gap at K', $|\tilde\Delta^+| < |\Delta^+| < |\varepsilon_F| < |\tilde\Delta^-|$.

    (iii) ε_F above the direct zone at K, but in the indirect zone at K', $|\Delta^+| < |\tilde\Delta^-| < |\varepsilon_F| < |\Delta^-|$.

    (iv) ε_F above the direct zones at K and K', $|\varepsilon_F| > \max\{|\Delta^+|, |\Delta^-|\}$.

(4) ε_F lying at overlapping indirect zones at K and K', $|\tilde\Delta^+| < |\tilde\Delta^-| < |\varepsilon_F| < |\Delta^+| < |\Delta^-|$.

Thus, from the spectral characteristics of the response of an individual valley it is possible to anticipate the spectral features of the total response. For example, in the case 1 the Hall conductivity will arise from the transverse response of the valley at K exclusively [Figs. 5(d)–5(f)], in the case 2 the spectrum will display features at the onsets $2\Delta^+$ and $2\Delta^-$, four critical frequencies will be present in the case 3(iv), while six will shape the spectrum in the case 4. To illustrate this variability of the optical response, in Fig. 6 we show $\sigma_{xy}(\omega)$ for the scenarios 2, 3(iv), and 4 only, in the name of brevity.

C. Drude weight

The intraband optical conductivity spectral weight is anisotropic, as expected, and shows a specific behavior due to the presence of unequal gaps. For gappless, tilted or untilted pair of cones, the Drude weight $D_{ii}^{(\xi)} \propto |\varepsilon_F|$, while for gapped graphene is $D_{\Delta^\xi} = \Theta(|\varepsilon_F| - |\Delta^\xi|)(e^2/\hbar^2)[\varepsilon_F^2 - (\Delta^\xi)^2]/|\varepsilon_F|$. In our case this behavior is modified in each valley because of the indirect nature of the gap. In addition, the breaking of the valley symmetry yields $D_{ii}^{(+)} \neq D_{ii}^{(-)}$. The total Drude weight $D_{ii} = \sum_\xi D_{ii}^{(\xi)}$ as a function of (positive) Fermi energy is shown in Fig. 7 for scenarios 1, 3, and 4. When the valley K' is gapless, its contribution to the total weight displays the characteristic linear dependence up to $\tilde\Delta^+$, after which the
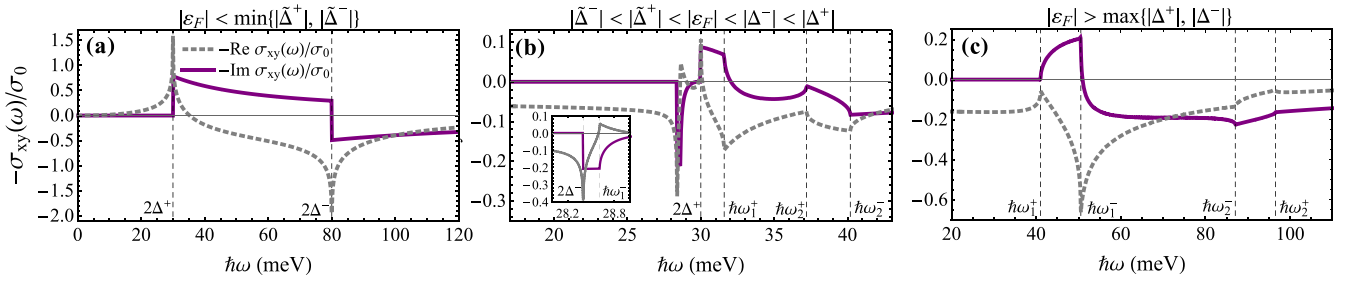
FIG. 6. Real and imaginary part of the total Hall response $\sigma_{xy}(\omega) = \sum_\xi \sigma_{xy}^{(\xi)}(\omega)$ for (a) Fermi level within the absolute gap, with $\Delta^+ = 15$ meV, $\Delta^- = 40$ meV, $\varepsilon_F = 0$ meV, (b) Fermi energy lying at overlapped indirect zones, with $\Delta^+ = 15$ meV, $\Delta^- = 14.2$ meV, $\varepsilon_F = 13.5$ meV, and (c) Fermi level above the direct zones $\Delta^+ = 15$ meV, for $\Delta^- = 25$ meV, $\varepsilon_F = 27$ meV.

contribution of the gapped valley K starts, presenting a specific nonlinear behavior in the indirect zone $\tilde{\Delta}^+ < \varepsilon_F < \Delta^+$, and a gapped-graphene-like D_{Δ^ξ} function above the nominal direct gap Δ^+ [Fig. 7(a)]. The situation looks rather different when both valleys are gapped. For the scenario with nonoverlapping indirect zones $|\tilde{\Delta}^+| < |\Delta^+| < |\tilde{\Delta}^-| < |\Delta^-|$ [Fig. 7(b)], $D_{ii}(\varepsilon_F)$ is zero for ε_F below $\tilde{\Delta}^+$, and then follows a behavior similar to that of Fig. 7(a) for $\tilde{\Delta}^+ < \varepsilon_F < \tilde{\Delta}^-$, determined only by transitions in the branch ε_+^+. Above $\tilde{\Delta}^-$, the transitions in the band ε_+^- are added, leading to a variation similar to that in Fig. 7(a). The function $D_{ii}(\varepsilon_F)$ notably changes when the indirect zones overlap, $\tilde{\Delta}^+ < \tilde{\Delta}^- < \Delta^+ < \Delta^-$ [Fig. 7(c)]. Between $\tilde{\Delta}^+$ and $\tilde{\Delta}^-$ only intraband transitions in the indirect zones of the branch ε_+^+ contribute, while for $\tilde{\Delta}^- < \varepsilon_F < \Delta^+$ transitions in the indirect zone of each valley start to count. In the range between Δ^+ and Δ^-, $D_{ii}^{(-)}$ is due to transitions in the band ε_+^- which take place only in the corresponding indirect zone. Above Δ^+ and Δ^-, the Drude weight behaves as can be identified in Fig. 7(a) or 7(b). Globally, a nonlinear dependence on ε_F, with an overall reduction of its magnitude, is observed for the total weight.

IV. OPTICAL PROPERTIES

A. Anisotropic response, circular dichroism, and valley polarization

The anisotropy expressed by the result $\sigma_{xx} \neq \sigma_{yy}$ can also be presented through the longitudinal conductivity $\sigma_\parallel(\omega; \varphi) = \sum_\xi \sigma_\parallel^{(\xi)}(\omega; \varphi)$. This scalar response function determines the density current induced along the direction of the external field, $\mathbf{J}_\parallel = \sigma_\parallel \mathbf{E}$, and it is given by $\sigma_\parallel(\omega; \varphi) =$

$\hat{q}_i \sigma_{ij}(\omega) \hat{q}_j$ (sum over repeated indices is implied), where $\hat{\mathbf{q}} = \cos\varphi\, \hat{\mathbf{x}} + \sin\varphi\, \hat{\mathbf{y}}$ gives the direction of the external field $\mathbf{E} \parallel \hat{\mathbf{q}}$. The quantity $\mathrm{Re}\,\sigma_\parallel(\omega; \varphi)$ determines the dissipation (power absorption/area) for linearly polarized fields. For the valley ξ,

$$\sigma_\parallel^{(\xi)}(\omega; \varphi) = \sigma_{xx}^{(\xi)}(\omega)\cos^2\varphi + \sigma_{yy}^{(\xi)}(\omega)\sin^2\varphi. \quad (26)$$

The off-diagonal components of the conductivity tensor does not appear in this quantity because of its antisymmetry, $\sigma_{yx}^{(\xi)} = -\sigma_{xy}^{(\xi)}$. Polar plots of the longitudinal conductivity Eq. (26), made of transitions in the vicinity of the valley $\xi = +$, are shown in Figs. 8(a)–8(c) as color maps for three positions of the level ε_F. We observe that, as a function of the direction φ, the response follows the same functional angular dependence as the function $g(\theta)$ when $|\varepsilon_F| < |\tilde{\Delta}^+|$ for frequencies above the gap, and when $|\varepsilon_F| > |\Delta^+|$ for $\omega > \omega_2^+$. Indeed, given that $\mathrm{Re}\,\sigma_{ii}^{(\xi)}(\omega) \propto \alpha_i^2$ we find that $\mathrm{Re}\,\sigma_\parallel^\xi(\omega; \varphi) = \bar{\sigma}(\omega)\Theta(\hbar\omega - 2|\Delta^\xi|)g^2(\varphi)$ for the former case [Fig. 8(a)] and $\mathrm{Re}\,\sigma_\parallel^\xi(\omega > \omega_2^\xi; \varphi) = \bar{\sigma}(\omega)g^2(\varphi)$ in the latter [Fig. 8(c)], where $\bar{\sigma}(\omega) = g_s(\sigma_0\pi/16)[1 + (2\Delta^\xi/\hbar\omega)^2]\alpha_F^2/\alpha_x\alpha_y$. This dependency on φ is otherwise modified for $\omega_1^\xi \leqslant \omega \leqslant \omega_2^\xi$ [Figs. 8(b) and 8(c)] due to the spectral characteristics of the allowed transitions in this frequency range. In Fig. 8(b), the anisotropy is hardly noticeable below $\hbar\omega_2^+$ because of the strong suppression of the spectrum there.

However, owing to the nonvanishing Hall component $\sigma_{xy}(\omega)$ the medium absorb right- and left-circularly polarized light differently, revealing the circular dichroism of the medium. The appropriate conductivity for circularly polarized external field $\mathbf{E}_\pm$ is the quantity $\sigma_\pm(\omega) =$
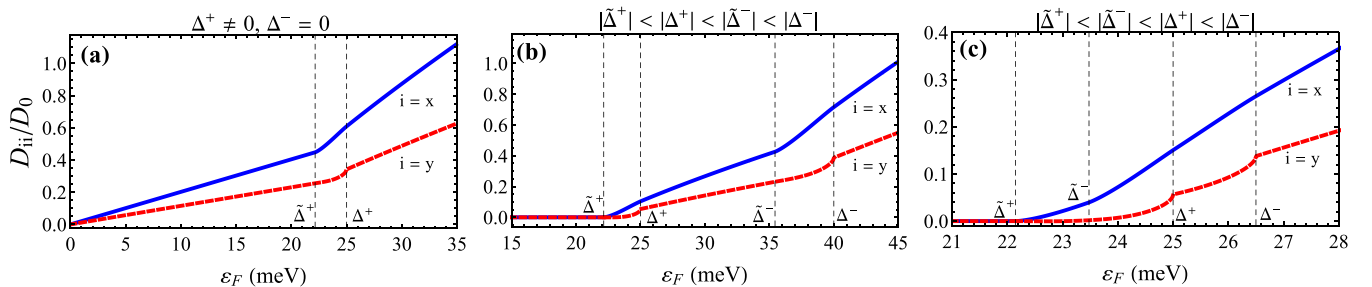

FIG. 7. Drude weight as a function of Fermi energy when $\Delta^+ = 25$ meV for (a) scenario 1, with $\Delta^- = 0$, (b) scenario 3, with $\Delta^- = 40$ meV, and (c) scenario 4, with $\Delta^- = 26.5$ meV. The scale is normalized to the Drude weight of pristine graphene $D_0 = (e^2/\hbar)(\varepsilon_F^0/\hbar)$, where $\varepsilon_F^0 = \hbar v_F \sqrt{\pi n_e}$ is the Fermi energy in pristine graphene, with electron density $n_e = 1 \times 10^{15}$ m^{-2}.
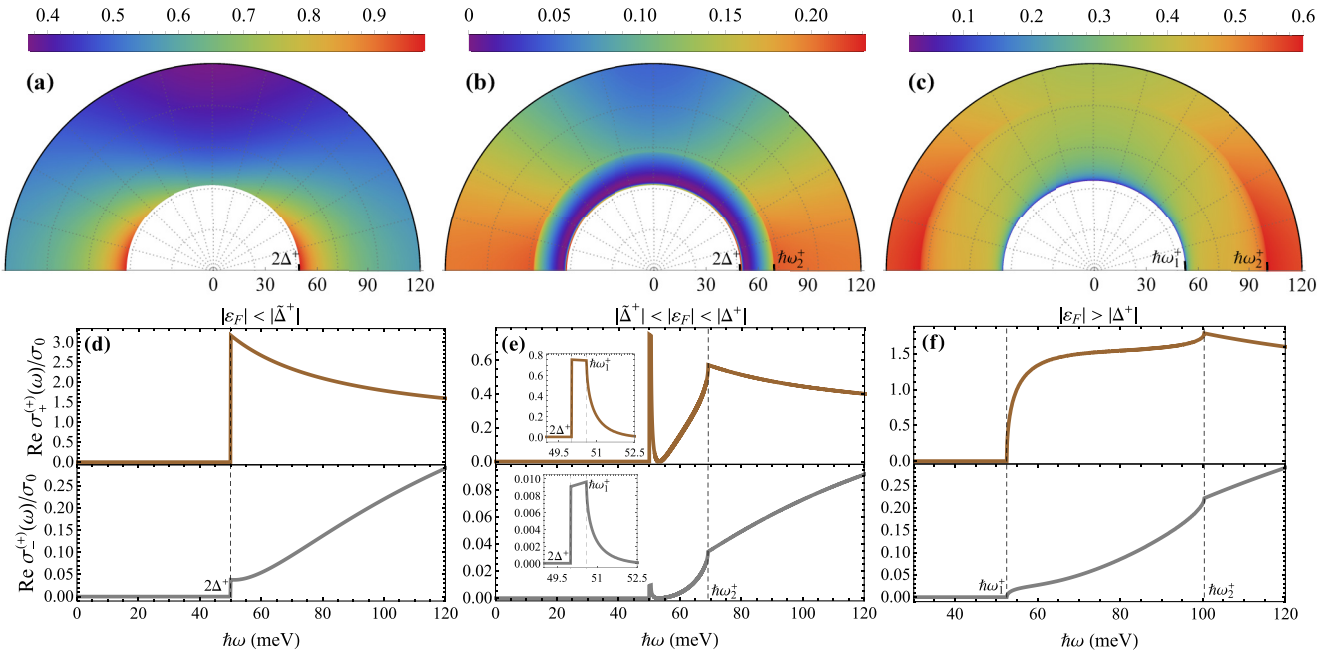
FIG. 8. Longitudinal conductivity $\text{Re}[\sigma_\parallel^{(+)}(\omega;\varphi)]$ (a–c) and circular dichroism response $\text{Re}[\sigma_\pm^{(+)}(\omega)]$ (d–f), for three distinct positions of the Fermi level in the vicinity of the K point with $\Delta^+ = 25$ meV.

$\sigma_{xx}(\omega) + \sigma_{yy}(\omega) \pm i[\sigma_{xy}(\omega) - \sigma_{yx}(\omega)]$, which gives the induced current $\mathbf{J} = \sigma_\pm \mathbf{E}_\pm$. In this case, the power absorption/ area is determined by

$$\text{Re}\,\sigma_\pm(\omega) = \text{Re}[\sigma_{xx}(\omega) + \sigma_{yy}(\omega)] \mp \text{Im}[\sigma_{xy}(\omega) - \sigma_{yx}(\omega)]. \quad (27)$$

Figures 8(d)–8(f) display $\text{Re}\,\sigma_+^{(+)}(\omega)$ and $\text{Re}\,\sigma_-^{(+)}(\omega)$ for several values of the level ε_F. As expected, for $|\varepsilon_F| < |\tilde{\Delta}^\xi|$ [Fig. 8(d)] and $|\varepsilon_F| > |\Delta^\xi|$ [Fig. 8(f)] the spectra show a graphenelike and borophenelike response, respectively [see Figs. 5(a), 5(c) 5(d), and 5(f)]. However, the new scenario [Fig. 8(e)] opened by the indirect nature of the gap [Fig. 8(e)] presents a spectrum which, in the interval $\omega_1^+ \leqslant \omega \leqslant \omega_2^+$, breaks that graphenelike behavior (observed in the narrow range $2\Delta^+ \leqslant \hbar\omega \leqslant \hbar\omega_1^+$) and the borophenelike behavior (started above ω_2^+).

Circular dichroism can also be illustrated through the Hall angle

$$\tan\Theta_H(\omega;\varepsilon_F) = \frac{\text{Re}\,\sigma_+ - \text{Re}\,\sigma_-}{\text{Re}\,\sigma_+ + \text{Re}\,\sigma_-} = \frac{-\text{Im}(\sigma_{xy} - \sigma_{yx})}{\text{Re}(\sigma_{xx} + \sigma_{yy})}. \quad (28)$$

In Fig. 9 we show the Hall angle spectrum as a function of the (positive) Fermi energy, encompassing the scenario 2 and the cases of scenario 3. When $\varepsilon_F < \tilde{\Delta}^+$ (scenario 2) the spectrum starts at the energy gap $2\Delta^+$, with decreasing magnitude until the onset $2\Delta^-$ where is an abrupt change of color due to a change of sign of $-\text{Im}[\sigma_{xy}(\omega)]$ [Fig. 6(a)]. For $\varepsilon_F > \Delta^-$ [case 3(iv)], the spectrum present four critical points, with a change of sign at ω_1^- [Fig. 6(c)]. When $\tilde{\Delta}^+ < \varepsilon_F < \Delta^+$ [case 3(i)], the angle $\Theta_H(\omega)$ show three critical points associated to the van Hove singularities of the JDOS in the indirect zone of the valley at K point, and a change of sign (from positive to negative) of $-\text{Im}[\sigma_{xy}(\omega)]$ at $2\Delta^-$. In contrast, at higher values of ε_F, lying within the other indirect zone [case 3(iii)], we see that the spectrum of dichroism will display five

critical energies, without any change of sign. With respect to the case 3(ii), where the Fermi level is outside the indirect zones but inside the K' valley gap, the corresponding spectrum is molded by three critical points and a change of sign of $-\text{Im}[\sigma_{xy}(\omega)]$.

We note that there are regions in the ε_F-ω diagram with the Hall angle close to $\pm\pi/4$ indicating an almost perfect circular dichroism, where the system absorbs mostly left circularly polarized light and very little the opposite handed polarization, or vice versa. Indeed, we note that for $\varepsilon_F < \tilde{\Delta}^+$ and $\hbar\omega \gtrsim 2\Delta^+$, the dichroism arises from the absorption at the K valley only. Thus $\text{Re}\,\sigma_\pm = \text{Re}\,\sigma_\pm^{(+)}$, where $\text{Re}\,\sigma_+^{(+)} \gg \text{Re}\,\sigma_-^{(+)}$, as can be seen in Fig. 8(d) for example, leading to $\tan\Theta_H \approx +1$. However, when $\tilde{\Delta}^+ < \varepsilon_F < \Delta^+ < \tilde{\Delta}^-$, $\text{Re}\,\sigma_- \approx \text{Re}\,\sigma_-^{(-)}$ and $\text{Re}\,\sigma_-^{(-)} \gg \text{Re}\,\sigma_+ = \text{Re}\,\sigma_+^{(+)} + \text{Re}\,\sigma_+^{(-)}$ for $\hbar\omega \gtrsim 2\Delta^-$, because of the decreasing of transitions at K valley [see Fig. 8(e)], leading to $\tan\Theta_H \approx -1$. This is remarkable because such possibility occurs due to the existence
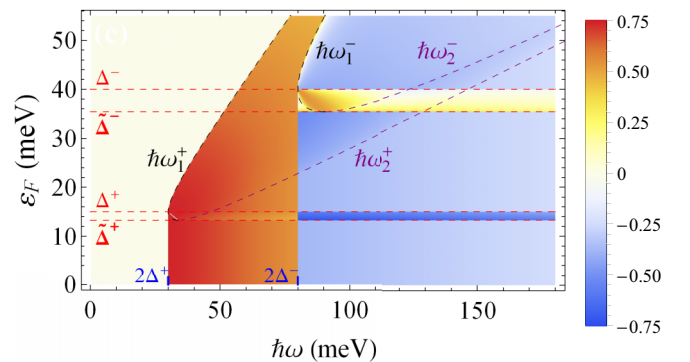

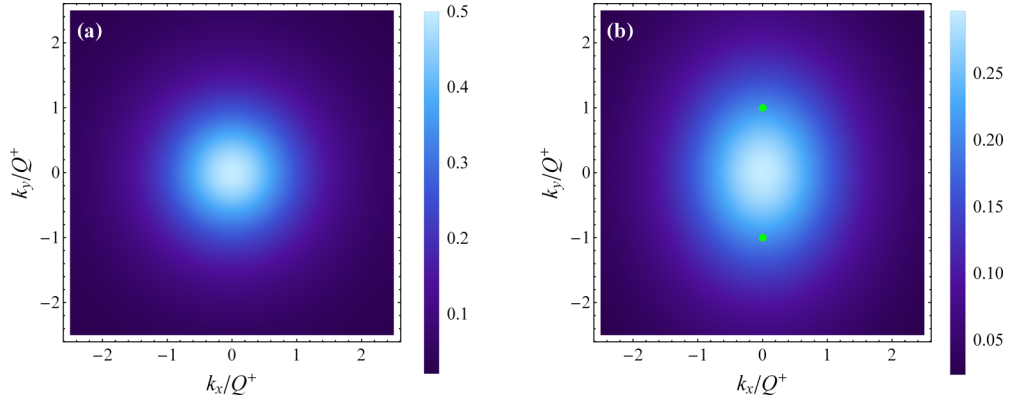FIG. 9. Hall angle $\Theta_H(\omega;\varepsilon_F)$ (radians), for $\Delta^+ = 15$ meV, $\Delta^- = 40$ meV.

FIG. 10. Berry curvature $-(\Delta^+/\alpha_F)^2\Omega^+_{+,z}(\mathbf{k})$ for the states in the band $\varepsilon^+_+(\mathbf{k})$ when (a) $v_t = 0$, $v_x = v_y$, and (b) $v_t \neq 0$, $v_x \neq v_y$; the points $(0, \pm Q^+)$ are indicated. We take $\Delta^+ = 25$ meV. The spread along k_y directions reflects the anisotropy of the band.

of an indirect zone and the associated significant reduction of the dynamical response. The result is in sharp contrast to the untilted case, where in a map like that of Fig. 9 only the value $\tan\Theta_H \approx +1$ can be achieved, for $\hbar\omega$ slightly above $2\Delta^+$.

It is interesting to consider the valley polarization expressed by the angle $\Theta_{V,\pm}$, which measures the difference of absorption of circularly polarized light between the K and K' valleys,

$$\tan\Theta_{V,\pm}(\omega; \varepsilon_F) = \frac{\operatorname{Re}\sigma^{(+)}_\pm - \operatorname{Re}\sigma^{(-)}_\pm}{\operatorname{Re}\sigma^{(+)}_\pm + \operatorname{Re}\sigma^{(-)}_\pm}. \tag{29}$$

As expected, for $\Delta^+ - \Delta^- = 0$, $\Theta_H = 0$ due to the TR invariance, and $\Theta_{V,\pm} \neq 0$ because of the breaking of inversion symmetry. Actually, under such conditions $\sigma^{(-)}_{xy} = -\sigma^{(+)}_{xy}$ and $\operatorname{Re}\sigma^{(\xi)}_\pm = \operatorname{Re}\sigma^{(-\xi)}_\mp$, implying that $\tan\Theta_{V,+} = -\tan\Theta_{V,-} = \operatorname{Re}[\sigma^{(+)}_+ - \sigma^{(+)}_-]/\operatorname{Re}[\sigma^{(+)}_+ + \sigma^{(+)}_-]$, which according to Fig. 8(d) gives $\tan\Theta_{V,\pm} \approx \pm\operatorname{sgn}(\Delta^+)$ for $\hbar\omega \gtrsim 2|\Delta^+|$. On the contrary, for $\Delta^+ + \Delta^- = 0$, $\Theta_{V,\pm} = 0$ and $\Theta_H \neq 0$ (with $\tan\Theta_H \approx \operatorname{sgn}(\Delta^+)$ for $\hbar\omega \gtrsim 2|\Delta^+|$) because TRS is broken in the system while retaining inversion symmetry. In the Haldane model, valley polarization and perfect circular dichroism have been reported to occur exclusively [70], while the possibility of simultaneous phenomena has been explored recently within a modified Haldane model [50]. In our model, for $|\Delta^+| \neq |\Delta^-|$ the valley polarization and circular dichroism are achieved simultaneously, suggesting an alternative tunable way to realize them.

B. Anomalous and valley Hall conductivities

The anomalous Hall conductivity (AHC) is defined by $\sigma^{\text{AHE}} = \sigma^{(+)}_{xy}(0) + \sigma^{(-)}_{xy}(0)$, which we obtain through the well-known formula

$$\sigma^{(\xi)}_{xy}(0) = -g_s \frac{e^2}{\hbar} \sum_\lambda \int \frac{d^2k}{(2\pi)^2} f[\varepsilon^\xi_\lambda(\mathbf{k})] \Omega^\xi_{\lambda,z}(\mathbf{k}), \tag{30}$$

where $\Omega^\xi_{\lambda,z}(\mathbf{k}) = -\xi\lambda\,\alpha_x\alpha_y\Delta^\xi/\{2[d^\xi(\mathbf{k})]^3\}$ is the Berry curvature of a state in the band ξ, λ. Note that $\Omega^\xi_{-,z} = -\Omega^\xi_{+,z}$. In contrast to gapped graphene [Fig. 10(a)], the curvature becomes smaller in magnitude, is no longer isotropic,

and spreads over the k_y-axis between the points $(0, \pm Q^\xi)$ [Fig. 10(b)].

At zero temperature, we have

$$\sigma^{\text{AHE}}(\varepsilon_F) = g_s \frac{e^2}{\hbar}\left[\int_{\mathcal{S}_+} \frac{d^2k}{(2\pi)^2} \Omega^+_{+,z}(\mathbf{k}) + \int_{\mathcal{S}_-} \frac{d^2k}{(2\pi)^2} \Omega^-_{+,z}(\mathbf{k})\right]$$

$$= -g_s \frac{e^2}{2\hbar}\alpha_x\alpha_y\left[\Delta^+ \int_{\mathcal{S}_+} \frac{d^2k}{(2\pi)^2} \frac{1}{(d^+(\mathbf{k}))^3}\right.$$

$$\left. - \Delta^- \int_{\mathcal{S}_-} \frac{d^2k}{(2\pi)^2} \frac{1}{(d^-(\mathbf{k}))^3}\right], \tag{31}$$

where the integrals are taken over the sets $\mathcal{S}_\xi = \{\mathbf{k}\,|\,\varepsilon^\xi_-(\mathbf{k}) < \varepsilon_F < \varepsilon^\xi_+(\mathbf{k})\}$. The breaking of the TRS (through $\Delta^+ \neq \Delta^-$) implies that $\Omega^-_{\lambda,z}(\mathbf{k}) \neq -\Omega^-_{\lambda,z}(-\mathbf{k})$ leading to $\sigma^{\text{AHE}} \neq 0$.

In the following, we show results for the scenarios made possible by the unequal gaps, mentioned above:

(1) $\Delta^+ \neq 0$, $\Delta^- = 0$, $\sigma^{\text{AHE}} = \sigma^{(+)}_{xy}(0)$.

(i) $|\varepsilon_F| < |\tilde{\Delta}^+|$

$$\frac{\sigma^{\text{AHE}}}{-(e^2/h)} = \operatorname{sgn}(\Delta^+), \tag{32}$$

where $\operatorname{sgn}(x)$ is the sign function. Thus a Hall plateau can be observed [46].

(ii) $|\tilde{\Delta}^+| < |\varepsilon_F| < |\Delta^+|$

$$\frac{\sigma^{\text{AHE}}}{-(e^2/h)} = \operatorname{sgn}(\Delta^+)\left(\frac{1}{2} - \frac{\beta_+}{\pi}\right) + \frac{\Delta^+}{\pi}\frac{\alpha_x}{\alpha_F}\frac{\alpha_y}{\alpha_F}\frac{\alpha_t}{\alpha_F}$$

$$\times \int_{\theta_0-\theta^*_+}^{\theta_0+\theta^*_+} d\theta\, \frac{\sin\theta}{g^2(\theta)} f(\theta; \Delta^+), \tag{33}$$

where

$$f(\theta; x) = \frac{\sqrt{\varepsilon_F^2 g^2(\theta) - x^2[g^2(\theta) - h^2(\theta)]}}{\varepsilon_F^2 g^2(\theta) + x^2 h^2(\theta)},$$

and β_+ is defined after Eq. (8).

(iii) $|\varepsilon_F| > |\Delta^+|$

$$\frac{\sigma^{\text{AHE}}}{-(e^2/h)} = \frac{\Delta^+}{\sqrt{\varepsilon_F^2 + \gamma^2(\Delta^+)^2}}. \tag{34}$$
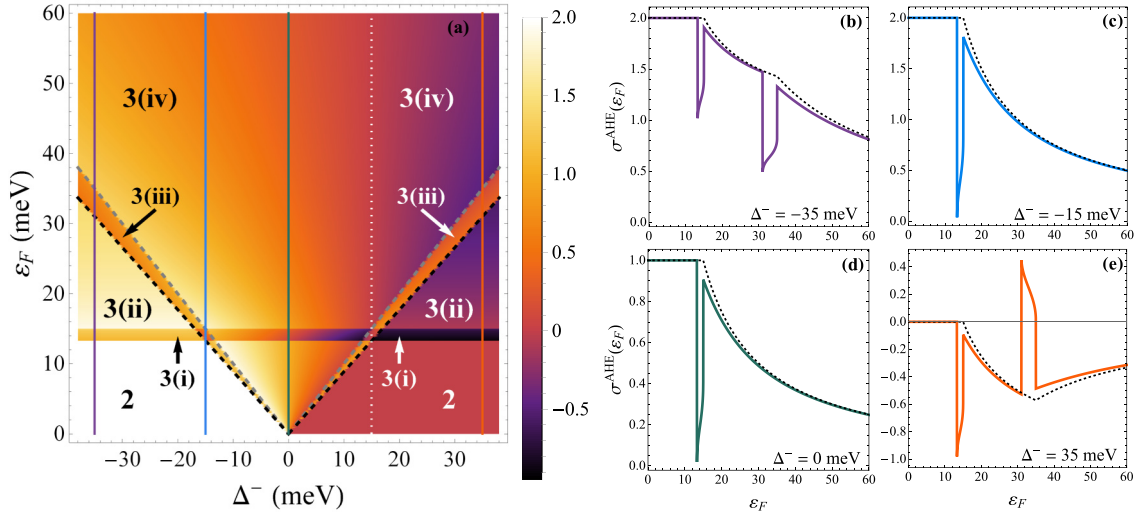
FIG. 11. (a) Contour map of the anomalous Hall conductivity (AHC) $\sigma^{\mathrm{AHE}}(\varepsilon_F; \Delta^-)$ (in units of $-e^2/h$), for $\Delta^+ = 15$ meV ($\tilde{\Delta}^+ = 13.3$ meV). Black dashed lines correspond to $\varepsilon_F = \pm\tilde{\Delta}^-$ and gray dashed lines to $\varepsilon_F = \pm\Delta^-$. The horizontal strip indicates the indirect zone $\tilde{\Delta}^+ < \varepsilon_F < \Delta^+$. The AHC vanishes along the vertical dotted line, defined by $\Delta^- = \Delta^+$. (b)-(e) Function $\sigma^{\mathrm{AHE}}(\varepsilon_F)$ for the values of the gap parameter Δ^- indicated by the vertical lines in (a). The dotted lines show the AHC of gapped graphene with $\Delta^- \neq \Delta^+$.

In the next, without loss of generality we shall take $|\Delta^+| < |\Delta^-|$:

(2) $|\varepsilon_F| < \min\{|\tilde{\Delta}^+|, |\tilde{\Delta}^-|\}$.

From Eq. (31),

$$\frac{\sigma^{\mathrm{AHE}}}{-(e^2/h)} = \mathrm{sgn}(\Delta^+) - \mathrm{sgn}(\Delta^-). \tag{35}$$

This expression was reported by Hill *et al.* [46] for gapped graphene with nonuniform gaps. According to the result Eq. (35), the anomalous conductivity can be zero or take the universal quantized value $\sigma^{\mathrm{AHE}} = \pm 2e^2/h$.

(3) $|\tilde{\Delta}^+| < |\Delta^+| < |\tilde{\Delta}^-| < |\Delta^-|$

(i) $|\tilde{\Delta}^+| < |\varepsilon_F| < |\Delta^+| < |\tilde{\Delta}^-| < |\Delta^-|$.

$$\frac{\sigma^{\mathrm{AHE}}}{-(e^2/h)} = \mathrm{sgn}(\Delta^+)\left(\frac{1}{2} - \frac{\beta_+}{\pi}\right) + \frac{\Delta^+}{\pi}\frac{\alpha_x}{\alpha_F}\frac{\alpha_y}{\alpha_F}\frac{\alpha_t}{\alpha_F}2$$
$$\times \int_{\theta_0 - \theta_+^*}^{\theta_0 + \theta_+^*} d\theta \frac{\sin\theta}{g^2(\theta)} f(\theta; \Delta^+) - \mathrm{sgn}(\Delta^-). \tag{36}$$

(ii) $|\tilde{\Delta}^+| < |\Delta^+| < |\varepsilon_F| < |\tilde{\Delta}^-| < |\Delta^-|$.

$$\frac{\sigma^{\mathrm{AHE}}}{-(e^2/h)} = \frac{\Delta^+}{\sqrt{\varepsilon_F^2 + \gamma^2(\Delta^+)^2}} - \mathrm{sgn}(\Delta^-). \tag{37}$$

(iii) $|\tilde{\Delta}^+| < |\Delta^+| < |\tilde{\Delta}^-| < |\varepsilon_F| < |\Delta^-|$.

$$\frac{\sigma^{\mathrm{AHE}}}{-(e^2/h)} = \frac{\Delta^+}{\sqrt{\varepsilon_F^2 + \gamma^2(\Delta^+)^2}} - \mathrm{sgn}(\Delta^-)\left(\frac{1}{2} - \frac{\beta_-}{\pi}\right)$$
$$- \frac{\Delta^-}{\pi}\frac{\alpha_x}{\alpha_F}\frac{\alpha_y}{\alpha_F}\frac{\alpha_t}{\alpha_F}\int_{\theta_0 - \theta_-^*}^{\theta_0 + \theta_-^*} d\theta \frac{\sin\theta}{g^2(\theta)} f(\theta; \Delta^-). \tag{38}$$

(iv) $|\tilde{\Delta}^+| < |\Delta^+| < |\tilde{\Delta}^-| < |\Delta^-| < |\varepsilon_F|$.

$$\frac{\sigma^{\mathrm{AHE}}}{-(e^2/h)} = \frac{\Delta^+}{\sqrt{\varepsilon_F^2 + \gamma^2(\Delta^+)^2}} - \frac{\Delta^-}{\sqrt{\varepsilon_F^2 + \gamma^2(\Delta^-)^2}}. \tag{39}$$

(4) $|\tilde{\Delta}^+| < |\tilde{\Delta}^-| < |\varepsilon_F| < |\Delta^+| < |\Delta^-|$.

$$\frac{\sigma^{\mathrm{AHE}}}{-(e^2/h)} = \left(\frac{1}{2} - \frac{\beta_+}{\pi}\right)\mathrm{sgn}(\Delta^+) - \left(\frac{1}{2} - \frac{\beta_-}{\pi}\right)\mathrm{sgn}(\Delta^-)$$
$$+ \frac{1}{\pi}\frac{\alpha_x}{\alpha_F}\frac{\alpha_y}{\alpha_F}\frac{\alpha_t}{\alpha_F}\left[\Delta^+ \int_{\theta_0 - \theta_+^*}^{\theta_0 + \theta_+^*} d\theta \frac{\sin\theta}{g^2(\theta)} f(\theta; \Delta^+)\right.$$
$$\left. - \Delta^- \int_{\theta_0 - \theta_-^*}^{\theta_0 + \theta_-^*} d\theta \frac{\sin\theta}{g^2(\theta)} f(\theta; \Delta^-)\right]. \tag{40}$$

In Fig. 11 we show the anomalous Hall conductivity as a function of Fermi energy for a continuous variation of Δ^-, at a given value of the gap at the K valley. Following Ref. [46], we consider positive and negative values of the quantities $\Delta^\pm$. Because σ^{AHE} Eq. (31) is an even function of ε_F we show only results for $\varepsilon_F \geqslant 0$. The labels on Fig. 11(a) indicate the region of each scenario, governed by the corresponding equation (for $|\Delta^-| > |\Delta^+|$). For instance, the regions marked by number 2 correspond to the Eq. (35), with $\mathrm{sgn}(\Delta^-) = -\mathrm{sgn}(\Delta^+)$ at the left, giving the universal value $-2e^2/h$ for the AHC, and $\mathrm{sgn}(\Delta^-) = \mathrm{sgn}(\Delta^+)$ at the right, giving a null value. The narrow strips labeled as 3(i) correspond to the AHC obtained from Eq. (36), while its magnitude in the triangular regions labeled as 3(ii) are given by Eq. (37), and so on. The AHC in the remaining regions which are not labeled, corresponding to the situation $|\Delta^-| < |\Delta^+|$, can be obtained from the same Eqs. (35)–(39) after the exchange $\Delta^- \leftrightarrow \Delta^+$. The small intersections between the narrow horizontal strip [3(i)] and the sectors marked as 3(iii) correspond to the case 4, Eq. (40), of overlapped indirect zones. We remark the need of the breaking of valley symmetry to have a finite Hall response [see Eq. (31)]. Indeed,
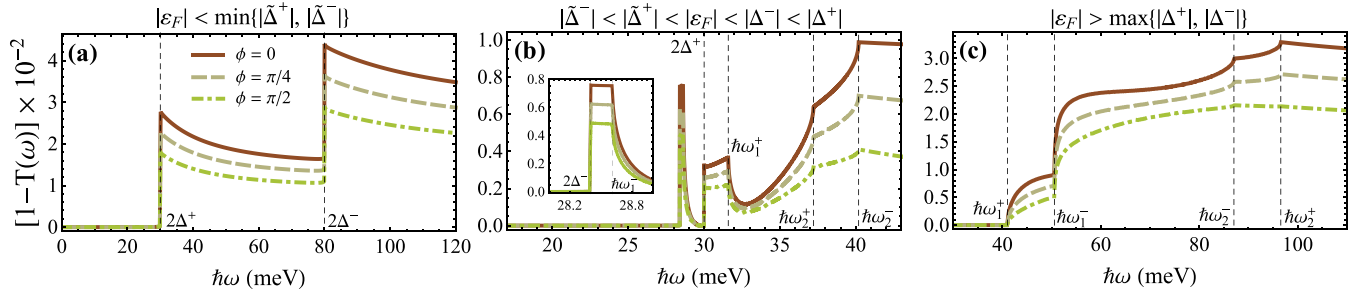
FIG. 12. Optical opacity $1 - T(\omega)$ for several values of the angle of polarization ϕ, at normal incidence ($\theta_i = 0$), and for the free-standing sample ($\epsilon_1 = \epsilon_2 = 1$). (a) Fermi level within the absolute gap (scenario 2), with $\Delta^+ = 15$ meV, $\Delta^- = 40$ meV, $\varepsilon_F = 0$ meV, (b) Fermi energy lying at overlapped indirect zones (scenario 4), with $\Delta^+ = 15$ meV, $\Delta^- = 14.2$ meV, $\varepsilon_F = 13.5$ meV, and (c) Fermi level above the direct zones (scenario 3(iv)) with $\Delta^+ = 15$ meV, $\Delta^- = 25$ meV, $\varepsilon_F = 27$ meV.

along the line $\Delta^- = \Delta^+$ [dotted line in (a)] the time-reversal symmetry is recovered and the AHC vanishes. Figures 11(b)–11(e) present the function $\sigma^{\text{AHE}}(\varepsilon_F)$ for several values of the gap parameter Δ^-, obtained by the vertical cuts indicated in the contour map. The magnitudes on the vertical cut at $\Delta^- = 0$ [green line in (a) and (d)] start in the universal value $-e^2/h$ [Eq. (32)], then takes a reduced value in the narrow strip [Eq. (33)], and decreases afterward according to Eq.(34). For gapped graphene with unequal gaps $\sigma^{\text{AHE}}/(-e^2/h) = \text{sgn}(\Delta^+) - \text{sgn}(\Delta^-)$ if $|\varepsilon_F| < \min\{|\Delta^+|, |\Delta^-|\}$, $(\Delta^+/|\varepsilon_F|) - \text{sgn}(\Delta^-)$ if $|\Delta^+| < |\varepsilon_F| < |\Delta^-|$, and $(\Delta^+ - \Delta^-)/|\varepsilon_F|$ if $|\varepsilon_F| > \max\{|\Delta^+|, |\Delta^-|\}$. For the sake of comparison, we have included in Figs. 11(b)–11(e) this result. We note that the main deviation from graphene behavior occurs due to the indirect zones, which are caused by the tilting and the mass in each valley.

Similar expressions to Eqs. (32)–(40) are derived for the conductivity response function $\sigma^{\text{VHE}} = \sigma_{xy}^{(+)}(0) - \sigma_{xy}^{(-)}(0)$, which characterizes the valley Hall effect. A contour map like that in Fig. 11(a) is obtained for the valley Hall conductivity (VHC) after a reflection in the line $\Delta^- = 0$. In particular, when $\Delta^+ + \Delta^- = 0$ the system presents inversion symmetry and a corresponding null valley Hall response. Moreover, the indirect zones introduce again the main modifications with respect to the valley response in the model of gapped graphene proposed by Hill *et al.* [46] ($\gamma = 0$, $v_x = v_y$).

C. Reflection and transmission

From the electromagnetic scattering problem of optical reflection and refraction at a flat interface made of a 2D system, with electrical conductivity σ_{ij}, separating two homogeneous media with dielectric constants ϵ_1 and ϵ_2, it is found that the optical reflectivity R and transmissivity T are given by

$$R(\omega, \theta_i, \phi; \varepsilon_F) = (|r_{pp}|^2 + |r_{sp}|^2) \cos^2 \phi + (|r_{ss}|^2 + |r_{ps}|^2)$$
$$\times \sin^2 \phi + 2 \text{Re}(r_{pp} r_{ps}^* + r_{ss} r_{sp}^*) \sin \phi \cos \phi, \tag{41}$$

$$T(\omega, \theta_i, \phi; \varepsilon_F) = F(\theta_i)[(|t_{pp}|^2 + |t_{sp}|^2) \cos^2 \phi + (|t_{ss}|^2 + |t_{ps}|^2)$$
$$\times \sin^2 \phi + 2 \text{Re}(t_{pp} t_{ps}^* + t_{ss} t_{sp}^*) \sin \phi \cos \phi], \tag{42}$$

where $F(\theta_i) = \sqrt{(\epsilon_2/\epsilon_1) - \sin^2 \theta_i}/\cos \theta_i$, θ_i is the angle of incidence and the angle of polarization ϕ is measured from the plane of incidence; p (s)-polarization corresponds to $\phi = 0$ ($\pi/2$). The coefficients $r_{\mu\nu}(\omega, \theta_i)$ [$t_{\mu\nu}(\omega, \theta_i)$] are the Fresnel reflection (transmission) amplitudes corresponding to a ν-polarized (p or s) incident wave generating a μ-polarized (p or s) reflected (transmitted) wave. In our problem, for the amplitudes involving polarization conversion we find $t_{sp} = r_{sp} = r_{ps} \propto \sigma_{xy}(\omega)$, and $t_{ps} = -\sqrt{\epsilon_2/\epsilon_1} \, r_{ps}/F(\theta_i) \propto \sigma_{xy}(\omega)$; for the conserved polarization cases, $t_{ss} = 1 + r_{ss}$, $t_{pp} = \sqrt{\epsilon_2/\epsilon_1}(1 - r_{pp})/F(\theta_i)$. Explicit expressions for the amplitudes $r_{\mu\nu}(\omega, \theta_i)$ are given in the Appendix B. We can expect that for $\mu = p$ or s incident polarization $R(\omega) \approx |r_{\mu\mu}(\omega)|^2$ and $T(\omega) \approx F(\theta_i)|t_{\mu\mu}(\omega)|^2$, and that their frequency dependence be mainly determined by $\sigma_{xx}(\omega) = \sum_\xi \sigma_{xx}^{(\xi)}(\omega)$ for $\mu = p$ and by $\sigma_{yy}(\omega) = \sum_\xi \sigma_{yy}^{(\xi)}(\omega)$ for $\mu = s$, given that $|\sigma_{xy}/c|^2 \ll 1$ [see Eqs. (B2)–(B5)].

This is illustrated in Fig. 12 where the frequency dependence of the optical opacity $1 - T(\omega; \phi)$ at normal incidence of a free-standing sample [$F(\theta_i) = 1$] is shown for several scenarios according to the position of the Fermi level and relative magnitudes of the gaps. Given that $R \sim 10^{-4}$, the absorbance $1 - T - R$ is determined to a large extent by that quantity. Approximately $1 - T(\omega) \approx (4\pi/c)\text{Re}[\sigma_{ii}(\omega)]$, with $i = x$ (y) for p (s)-polarization. Indeed, in Fig. 12 the form of the function $\sigma_{xx}^{(\xi)}(\omega)$ for $\phi = 0$ or of $\sigma_{yy}^{(\xi)}(\omega)$ for $\phi = \pi/2$ can be easily identified after Figs. 5(a)–5(c). When ε_F lies in the gaps,

$$1 - T(\omega) \approx \frac{\pi\alpha}{2} \frac{v_i^2}{v_x v_y} \left\{ \left[1 + \left(\frac{2\Delta^+}{\hbar\omega} \right)^2 \right] \Theta(\hbar\omega - 2|\Delta^+|) \right.$$
$$\left. + \left[1 + \left(\frac{2\Delta^-}{\hbar\omega} \right)^2 \right] \Theta(\hbar\omega - 2|\Delta^-|) \right\}, \tag{43}$$

where $\alpha = e^2/\hbar c$ is the fine structure constant. For $\varepsilon_F > \max\{|\Delta^+|, |\Delta^-|\}$, with $\omega > \max\{\omega_2^+, \omega_2^-\}$,

$$1 - T(\omega) \approx \frac{\pi\alpha}{2} \frac{v_i^2}{v_x v_y} \left[2 + \left(\frac{2\Delta^+}{\hbar\omega} \right)^2 + \left(\frac{2\Delta^-}{\hbar\omega} \right)^2 \right]. \tag{44}$$

For high enough frequencies, these results tends both to $(2.3\%)(v_i^2/v_x v_y)$, where the value $\pi\alpha = 2.3\%$ is the well-known visual transparency of pristine graphene, defined only
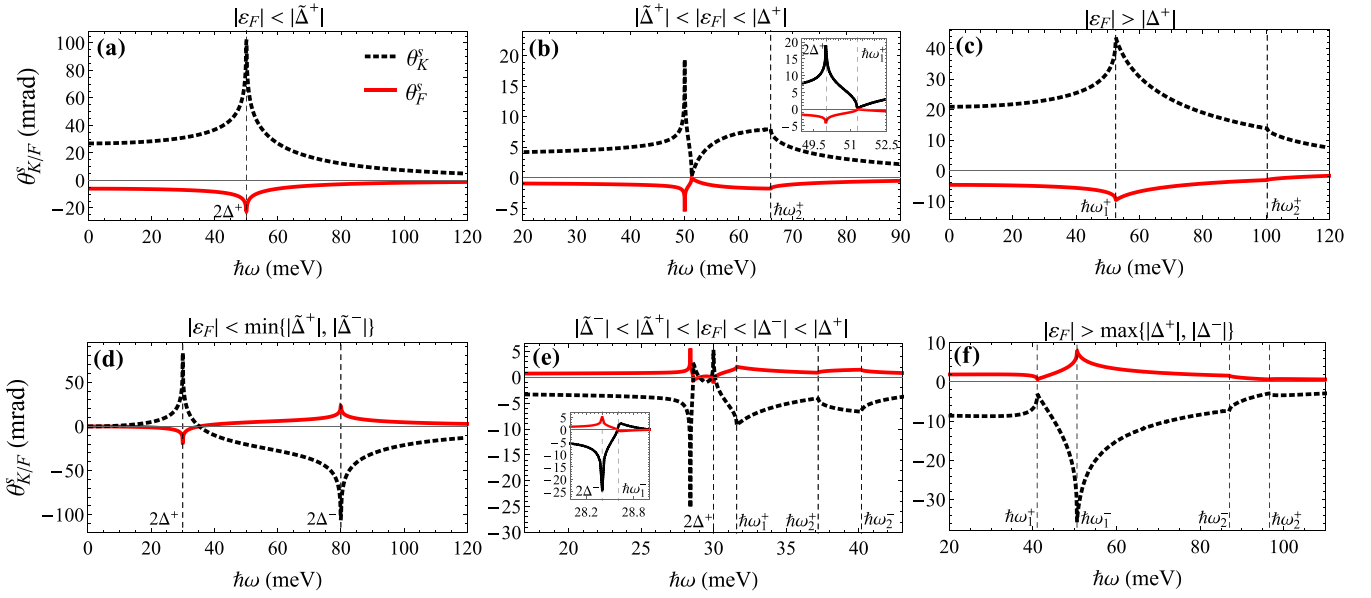
FIG. 13. Kerr and Faraday rotations $\theta^s_{K/F}$ at normal incidence ($\theta_i = 0$), and considering $\epsilon_1 = 1$, $\epsilon_2 = 2$ (SiO$_2$). In (a–c) it is considered $\Delta^+ = 25$ meV and $\Delta^- = 0$, for different positions of the Fermi level as shown. (d) Fermi level within the absolute gap (scenario 2), with $\Delta^+ = 15$ meV, $\Delta^- = 40$ meV, $\varepsilon_F = 0$ meV, (e) Fermi energy lying at overlapped indirect zones (scenario 4), with $\Delta^+ = 15$ meV, $\Delta^- = 14.2$ meV, $\varepsilon_F = 13.5$ meV, and (f) Fermi level above the direct zones (scenario 3(iv)) with $\Delta^+ = 15$ meV, $\Delta^- = 25$ meV, $\varepsilon_F = 27$ meV.

by fundamental constants [2]. That limit values are close to 2.9% for $i = x$ and 1.8% for $i = y$. In Fig. 12(a), for p-polarization at $\hbar\omega \gtrsim 2\Delta^+$ and $\hbar\omega \gtrsim 2\Delta^-$, $1 - T \approx 2.9\%$ and 4.5% for $i = x$, and 1.8% and 2.9% for $i = y$, respectively. Comparable values are obtained in Fig. 12(c) at $\omega^\pm_2$. However, for ε_F within overlapping indirect zones the transmission increases, as expected, with $1 - T(\omega) < 1\%$ [Fig. 12(b)]. For $\epsilon_2 > 1$ the opacity increases. As an example, we obtain $1 - T(\omega) \lesssim 3.8\%$ for the scenario of Fig. 12(b) when $\epsilon_2 = 2$.

D. Rotation of polarization

The breaking of the time reversal symmetry and the concomitant finite value of a transverse response lead to the well known phenomenon of polarization rotation of reflected and transmitted optical waves. The Kerr (K) and Faraday (F) angles giving the azimuth of the ellipse of polarization can be obtained from the expression

$$\tan 2\theta^\alpha_{K/F} = \frac{2\mathrm{Re}\{\chi^\alpha_{K/F}\}}{1 - |\chi^\alpha_{K/F}|^2}, \tag{45}$$

where $\alpha = p\,(s)$ indicates the incident linearly $p\,(s)$-polarized light, $\chi^p_K = -r_{sp}/r_{pp}$, $\chi^s_K = r_{ps}/r_{ss}$ for the reflected light, and $\chi^p_F = t_{sp}/t_{pp}$, $\chi^s_F = -t_{ps}/t_{ss}$ for the transmitted light. Typically, $|\chi^\alpha_{K/F}| \ll 1$ and $\theta^\alpha_{K/F} \approx \mathrm{Re}\{\chi^\alpha_{K/F}\}$.

Figure 13 shows results for $\theta^s_{K/F}(\omega)$ for three different positions of the Fermi energy when the K' valley is gapless (top panels), and for the scenarios 2, 4, and 3(iv) (bottom panels). We consider normal incidence, and $\epsilon_1 = 1$, $\epsilon_2 = 2$. We note that the frequency dependence of these angles follows mainly that of the function $-\mathrm{Re}[\sigma_{xy}(\omega; \varepsilon_F)]$ (see Fig. 6). Indeed, given the smallness of $|\sigma_{ii}|/c$ and $(|\sigma_{xy}|/c)^2$, we find

$\theta^p_{K/F}(\omega) \approx \theta^s_{K/F}(\omega)$, and as a good approximation

$$\theta^s_K(\omega) \approx -\frac{8\pi\,\mathrm{Re}[\sigma_{xy}(\omega)/c]}{\epsilon_2 - 1 + 2\pi\alpha\sqrt{\epsilon_2}},$$

$$\theta^s_F(\omega) \approx \frac{4\pi\,\mathrm{Re}[\sigma_{xy}(\omega)/c]}{\sqrt{\epsilon_2} + 1 + \pi\alpha},$$

after taking $\sigma_{ii}/c \approx \pi\sigma_0/4c = \alpha/4$. As expected, near the resonances the Kerr and Faraday rotations increases, reaching magnitudes $\sim 10^{-2} - 10^{-1}$ rad and $\sim 10^{-3} - 10^{-2}$ rad, respectively. Note also that at low frequency $\theta^s_{K/F}(0)$ is determined approximately by σ^{AHE}. In the valley symmetry breaking mechanism suggested for graphene by Hill *et al.* [46], a periodic magnetic flux opens gaps at both valleys which can be tuned independently. In our case, that mechanism would allow to change the sign of Δ^- leading to $\theta^s_{K/F}(0) \approx \sigma^{\mathrm{VHE}}$.

Figure 14(a) shows the Kerr rotation as a function of the incident angle, when the Fermi level lies within the gaps, at a frequency close to the onset for interband transitions at the K' valley, $\hbar\omega \approx 2\Delta^-$. There is a strong enhancement of the rotation, about $\pi/2$, for an incident angle defined approximately by $(\sqrt{\epsilon_2}/\cos\theta_t) - (\sqrt{\epsilon_1}/\cos\theta_i) = -(4\pi/c)\sigma_{xx}(\omega)$, where θ_t is determined by the Snell's law (Appendix B). That angle is very close to the Brewster value given by $\tan\theta_B = \sqrt{\epsilon_2/\epsilon_1}$. At $\theta_i = \theta_B$ we find

$$\chi^p_K(\omega; \theta_B) \approx -\frac{2\sqrt{\epsilon_1}\sigma_{xy}}{\sqrt{\epsilon_1 + \epsilon_2}\,\sigma_{xx} + \frac{4\pi}{c}\left(\sigma_{xx}\sigma_{yy} + \sigma^2_{xy}\right)}, \tag{46}$$

which can be further approximated by $\chi^p_K \approx -2\cos\theta_B(\sigma_{xy}/\sigma_{xx})$; the Kerr angle is found from Eq. (45). An enhancement close to the Brewster angle has also been reported for bilayer graphene in the quantum anomalous Hall state [10].
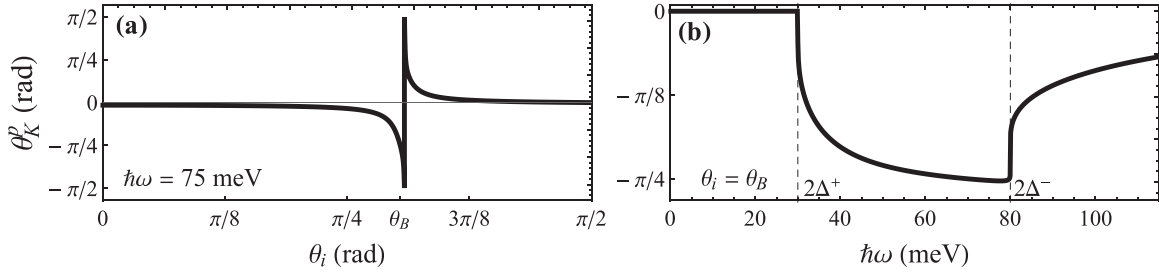
FIG. 14. Kerr rotation $\theta_K^p(\omega, \theta_i)$ for Fermi level within the gap of the system, $\varepsilon_F < \min\{|\tilde{\Delta}^+|, |\tilde{\Delta}^-|\}$ (scenario 2), with $\Delta^+ = 15$ meV, $\Delta^- = 40$ meV, $\varepsilon_F = 0$ meV, and $\epsilon_1 = 1$, $\epsilon_2 = 2$ (SiO$_2$). (a) Kerr angle as a function of the angle of incidence, at $\hbar\omega = 75$ meV, close to the onset $2\Delta^-$. For $\theta_i \approx \theta_B$, $\theta_K^p \approx \pi/2$. (b) Kerr angel spectrum at $\theta_i = \theta_B$.

In Fig. 14(b) the spectrum for the Kerr rotation at $\theta_i = \theta_B$ is displayed. For low frequencies, below the onsets of interband transitions, the conductivity response is determined by the dispersive components. Indeed, σ_{xy} is a real quantity while σ_{xx} becomes imaginary, yielding $\text{Re}(\sigma_{xy}/\sigma_{xx}) \approx 0$ and a small value for the Kerr rotation. Above $2\Delta^+$, the optical transitions in the K valley increase the dissipative components $\text{Re}(\sigma_{xx}^{(+)})$ and $\text{Im}(\sigma_{xy}^{(+)})$, implying that the relative phase of σ_{xy} and σ_{xx} becomes increasingly small. Accordingly, the angle θ_K^p starts to increase in magnitude and takes its largest (negative) value for $\hbar\omega \lesssim 2\Delta^-$, when the complex quantities σ_{xy} and σ_{xx} are closely in phase. However, for $\hbar\omega > 2\Delta^-$ the Kerr angle decreases in magnitude again for increasing frequency. This is due to the fact that the optical transitions at both valleys start to contribute, and for high enough frequency $\sigma_{xy} \approx i\text{Im}(\sigma_{xy})$ and $\sigma_{xx} \approx \text{Re}(\sigma_{xx})$ become out of phase.

The characteristic spectral features displayed by these results provide fingerprints of the anomalous transverse response, and suggest optical polarization rotation measurements as a contact-free probe of the valley symmetry breaking in the presence of tilting.

V. SUMMARY AND CONCLUSIONS

Following the study of Hill *et al.* [46] about a mechanism to break the valley symmetry in graphene and tune the gaps independently, we explored the effect of valley-contrasting gaps on the optical properties of two-dimensional anisotropic tilted Dirac systems like 8-*Pmmn* borophene and some organic conductors. We employed a low-energy effective Hamiltonian with broken particle-hole and valley symmetries. The energy spectrum is characterized by a valley index and the helicity of the states. Notably, the energy bands develop an indirect gap $2\tilde{\Delta}^\xi = 2\Delta^\xi \sqrt{1 - \gamma^2}$ in each valley, which is lower than the nominal gap $2\Delta^\xi$ of the untilted system and depends on the tilting and anisotropy through the parameter $\gamma = v_t/v_y$. As a consequence, when the Fermi level is outside a gap but close to the band edge of each valley, the corresponding Fermi contours can be displaced enough to provoke a dramatic change of the momentum space available for optical transitions. To explore this, we first calculated the joint density of states to probe the spectrum of interband transitions. When the Fermi energy lies within a gap, the JDOS displays the characteristic linear frequency dependence above the only critical energy defined by the onset $2\Delta^\xi$. However, if the Fermi level is above $2\tilde{\Delta}^\xi$, then the behavior of JDOS is no longer like that

of graphene with the usual threshold at $\hbar\omega = 2\varepsilon_F$ but looks qualitatively similar to that of borophene case, presenting two critical energies made possible by the tilt of the bands. However, given the new possibility of an indirect range $\tilde{\Delta}^\xi < \varepsilon_F < \Delta^\xi$, we found that the JDOS presents now three van Hove singularities in that range, and a strong reduction of the number of vertical transitions in a subregion located between photon energy intervals with graphenelike and borophenelike behaviors. Accordingly, the intraband and interband parts of the optical conductivity tensor were also obtained from the Kubo formula. We found an anisotropic response $\sigma_{xx}^{(\xi)}(\omega) \neq \sigma_{yy}^{(\xi)}(\omega)$ and a finite Hall component $\sigma_{xy}^{(\xi)}(\omega)$ with spectral features determined by the set of interband critical points revealed by the JDOS. When the contributions of each valley are combined to obtain the total response, a number of spectra are obtained because of the multiple possibilities for the position of the Fermi level in the complete set of bands, opened by the presence of nonuniform gaps. Similarly, the Drude weight is anisotropic and shows a sensitive dependence on the Fermi energy. To further characterize this scenario, we also calculated the anomalous and valley Hall conductivities through the Berry curvature of the bands, and spectra of circular dichroism, optical opacity, and Kerr and Faraday angles of polarization rotation. The plots of the AHC and VHC versus Fermi energy show behaviors that differ appreciably from the case without tilting due to the presence of indirect zones. Moreover, when the Fermi level is inside the absolute gap they can take universal values. Interestingly, we found that the existence of indirect zones makes possible to have almost perfect circular dichroism for right or left handed polarized light. Valley polarization can appear simultaneously, as recently reported within a modified Haldane model. With respect to the rotation of polarization, the Kerr and Faraday spectra display a strong dependence on the position of the Fermi level, signaled by the van Hove singularities of the JDOS, and reaching magnitudes about 10^{-3}–10^{-2} rad and 10^{-2}–10^{-1} rad, respectively. We observed an enhancement of Kerr rotation close to the Brewster angle of incidence, similar to that reported for bilayer graphene in the anomalous Hall state. We also found that by choosing appropriately the Fermi level position and tuning the exciting frequency close to the interband critical points, the optical transparency can deviate from the well known universal result $\pi e^2/\hbar c = 2.3\%$ of graphene by a factor that depends on the velocities v_x, v_y and gap parameters. We note that, qualitatively, the same kind of optical properties are obtained when these parameters are

varied, whenever the global shape of the energy bands is preserved.

In summary, the results show clear optical signatures of valley and electron-hole symmetry breaking in the optical properties, suggesting diverse optical ways to explore the simultaneous presence of anisotropy, tilt, and nonuniform gaps in Dirac systems.

APPENDIX A: FERMI LINES

(1) For $|\varepsilon_F| > |\Delta^\xi|$, the equation $\varepsilon_\lambda^\xi(k, \theta) = \lambda|\varepsilon_F|$ yields the parametric curve

$$k_{\lambda,F}^\xi(\theta) = \frac{1}{\alpha_F} \frac{\sqrt{E(\theta)} - \xi\lambda|\varepsilon_F|h(\theta)}{g^2(\theta) - h^2(\theta)} \qquad (A1)$$

for $\theta \in [0, 2\pi]$, where $E(\theta) = \varepsilon_F^2 g^2(\theta) - (\Delta^\xi)^2[g^2(\theta) - h^2(\theta)]$. The energy difference $\varepsilon_+^\xi(k, \theta) - \varepsilon_-^\xi(k, \theta) = 2d^\xi(k, \theta)$ at the Fermi curve is denoted by $\hbar\omega_\lambda^\xi(\theta) = 2d^\xi[k_{\lambda,F}^\xi(\theta), \theta]$, and given by

$$\hbar\omega_\lambda^\xi(\theta) = 2\frac{|\varepsilon_F|g^2(\theta) - \xi\lambda h(\theta)\sqrt{E(\theta)}}{g^2(\theta) - h^2(\theta)}. \qquad (A2)$$

(2) For $|\tilde{\Delta}^\xi| \leqslant |\varepsilon_F| \leqslant |\Delta^\xi|$, the Fermi line is given by the parametric curve

$$q_{\lambda,F}^{\xi,\pm}(\theta) = \frac{1}{\alpha_F} \frac{\xi\lambda|\varepsilon_F|[-h(\theta)] \pm \sqrt{E(\theta)}}{g^2(\theta) - h^2(\theta)}, \qquad (A3)$$

defined in the angular regions $|\theta - \theta_0| \leqslant \theta_\xi^*$, where $\theta_0 = 3\pi/2$ if $\xi\lambda = +$ and $\pi/2$ when $\xi\lambda = -$. The angle θ_ξ^* is defined by the condition $E(\theta) \geqslant 0$. Correspondingly, the energy difference between the conduction and valence band at the Fermi curve is $\hbar\nu_\lambda^{\xi,\pm}(\theta) = 2d^\xi(q_{\lambda,F}^{\xi,\pm}(\theta), \theta)$. Explicitly,

$$\hbar\nu_\lambda^{\xi,\pm}(\theta) = 2\frac{|\varepsilon_F|g^2(\theta) \pm \xi\lambda[-h(\theta)]\sqrt{E(\theta)}}{g^2(\theta) - h^2(\theta)}, \qquad (A4)$$

with $\hbar\nu_\lambda^{\xi,+}(\theta) > \hbar\nu_\lambda^{\xi,-}(\theta)$.

APPENDIX B: FRESNEL AMPLITUDES

Here we sketch the solution of the electromagnetic problem defined in Sec. IV C. We consider harmonic plane waves $\mathbf{F}(\mathbf{r}, t) = \mathbf{F}(\mathbf{r})e^{-i\omega t}$ with $\mathbf{F}(\mathbf{r}) = \mathbf{F}e^{i\mathbf{k}\cdot\mathbf{r}}$ satisfying the Helmholtz equation $(\nabla^2 + n^2 k_0^2)\mathbf{F}(\mathbf{r}) = 0$, where the wave vector $\mathbf{k} = nk_0\hat{\mathbf{k}}$ lies in the ZX plane, $\mathbf{k} \cdot \mathbf{F} = 0$, $k_0 = \omega/c$, and $n = \sqrt{\epsilon}$ is the index of refraction. It is convenient to introduce two vectors perpendicular to $\hat{\mathbf{k}}$ to span the vectorial amplitude $\mathbf{F}$. One of these vector is $\hat{\mathbf{s}} = \hat{\mathbf{z}} \times \hat{\mathbf{x}} = \hat{\mathbf{y}}$; for the other we can take $\hat{\mathbf{p}} = \hat{\mathbf{s}} \times \hat{\mathbf{k}}$. Thus, we have defined the (real) orthogonal triad $(\hat{\mathbf{p}}, \hat{\mathbf{s}}, \hat{\mathbf{k}})$ as a basis to describe transverse plane waves. The incident electric field $\mathbf{F} = \mathbf{E}^i$ from the medium with dielectric constant ϵ_1 is then written in terms of its p and s amplitudes as $\mathbf{E}^i = E_p^i\hat{\mathbf{p}}^i + E_s^i\hat{\mathbf{s}}$, where $\hat{\mathbf{p}}^i = \hat{\mathbf{s}} \times \hat{\mathbf{k}}^i = \frac{1}{k^i}(k_z^i\hat{\mathbf{x}} - k_x\hat{\mathbf{z}}) = \cos\theta_i\hat{\mathbf{x}} - \sin\theta_i\hat{\mathbf{z}}$ and $\mathbf{k}^i = k_0\sqrt{\epsilon_1}\hat{\mathbf{k}}^i = k_x\hat{\mathbf{x}} + k_z^i\hat{\mathbf{z}} = k_0\sqrt{\epsilon_1}(\sin\theta_i\hat{\mathbf{x}} + \cos\theta_i\hat{\mathbf{z}})$ are the polarization vector and wave vector of the incident wave, with $k^i = k_0\sqrt{\epsilon_1}$ and θ_i being the angle of incidence. Similarly, the reflected field is $\mathbf{E}^r = E_p^r\hat{\mathbf{p}}^r + E_s^r\hat{\mathbf{s}}$, where $\hat{\mathbf{p}}^r = \hat{\mathbf{s}} \times \hat{\mathbf{k}}^r = \frac{1}{k^i}(-k_z^r\hat{\mathbf{x}} - k_x\hat{\mathbf{z}}) = -\cos\theta_i\hat{\mathbf{x}} - \sin\theta_i\hat{\mathbf{z}}$ and $\mathbf{k}^r = k_0\sqrt{\epsilon_1}\hat{\mathbf{k}}^r = k_x\hat{\mathbf{x}} - k_z^r\hat{\mathbf{z}} = k_0\sqrt{\epsilon_1}(\sin\theta_i\hat{\mathbf{x}} - \cos\theta_i\hat{\mathbf{z}})$; note that $k_z^r = k_z^i = k_0\sqrt{\epsilon_1}\cos\theta_i$. In the medium ϵ_2, the transmitted field reads as $\mathbf{E}^t = E_p^t\hat{\mathbf{p}}^t + E_s^t\hat{\mathbf{s}}$, with $\hat{\mathbf{p}}^t = \hat{\mathbf{s}} \times \hat{\mathbf{k}}^t = \frac{1}{k^t}(k_z^t\hat{\mathbf{x}} - k_x\hat{\mathbf{z}}) = \cos\theta_t\hat{\mathbf{x}} - \sin\theta_t\hat{\mathbf{z}}, \mathbf{k}^t = k_0\sqrt{\epsilon_2}\hat{\mathbf{k}}^t = k_x\hat{\mathbf{x}} + k_z^t\hat{\mathbf{z}} = k_0\sqrt{\epsilon_2}(\sin\theta_t\hat{\mathbf{x}} + \cos\theta_t\hat{\mathbf{z}}), k^t = k_0\sqrt{\epsilon_2}$; the angle of refraction θ_t is determined by the Snell's law $k_x^i = k_x^t$: $\sqrt{\epsilon_1}\sin\theta_i = \sqrt{\epsilon_2}\sin\theta_t$. The corresponding magnetic fields are $\mathbf{B}^a = \frac{1}{k_0}\mathbf{k}^a \times \mathbf{E}^a$, $a = i, r, t$.

The reflected and transmission amplitudes $E_{p,s}^r, E_{p,s}^t$ can be written in terms of Fresnel amplitudes $r_{\mu\nu}, t_{\mu\nu}$,

$$\begin{pmatrix} E_p^r \\ E_s^r \end{pmatrix} = \begin{pmatrix} r_{pp} & r_{ps} \\ r_{sp} & r_{ss} \end{pmatrix}\begin{pmatrix} E_p^i \\ E_s^i \end{pmatrix}, \qquad \begin{pmatrix} E_p^t \\ E_s^t \end{pmatrix} = \begin{pmatrix} t_{pp} & t_{ps} \\ t_{sp} & t_{ss} \end{pmatrix}\begin{pmatrix} E_p^i \\ E_s^i \end{pmatrix} \qquad (B1)$$

(in the basis $\{\hat{\mathbf{p}}, \hat{\mathbf{s}}\}$). They should satisfy the boundary conditions (1) $\hat{\mathbf{z}} \cdot [\epsilon_2\mathbf{E}^t - \epsilon_1(\mathbf{E}^i + \mathbf{E}^r)] = 4\pi\sigma_s(\omega)$, (2) $\hat{\mathbf{z}} \times [\mathbf{E}^t - (\mathbf{E}^i + \mathbf{E}^r)] = \mathbf{0}$, (3) $\hat{\mathbf{z}} \cdot [\mathbf{B}^t - (\mathbf{B}^i + \mathbf{B}^r)] = 0$, and (4) $\hat{\mathbf{z}} \times [\mathbf{B}^t - (\mathbf{B}^i + \mathbf{B}^r)] = \frac{4\pi}{c}\mathbf{J}_s(\omega)$, where the induced surface charge density σ_s is related to the surface current $J_{s,i}(\omega) = \sigma_{ij}(\omega)E_j(z=0)$, $i, j = x, y$, through the continuity equation, which implies $k_x J_{s,x}(\omega) = \omega\sigma_s(\omega)$. Given that $E_x(z=0) = E_x^i(0) + E_x^r(0) = E_x^t(0) = (k_z^t/k^t)E_p^t = (k_z^i/k^i)(E_p^i - E_p^r)$ and $E_y(z=0) = E_y^i(0) + E_y^r(0) = E_y^t(0) = E_s^t = E_s^i + E_s^r$,

$$J_{s,x}(\omega) = \sigma_{xx}(\omega)\frac{k_z^t}{k^t}E_p^t + \sigma_{xy}(\omega)E_s^t = \sigma_{xx}(\omega)\frac{k_z^i}{k^i}(E_p^i - E_p^r) + \sigma_{xy}(\omega)(E_s^i + E_s^r),$$

$$J_{s,y}(\omega) = \sigma_{yx}(\omega)\frac{k_z^t}{k^t}E_p^t + \sigma_{yy}(\omega)E_s^t = \sigma_{yx}(\omega)\frac{k_z^i}{k^i}(E_p^i - E_p^r) + \sigma_{yy}(\omega)(E_s^i + E_s^r).$$

The algebraic system of equations defined by the boundary conditions can be rearranged, leading to

$$\begin{pmatrix} M_{pp} & M_{ps} \\ M_{sp} & M_{ss} \end{pmatrix}\begin{pmatrix} E_p^r \\ E_s^r \end{pmatrix} = \begin{pmatrix} F_{pp} & F_{ps} \\ F_{sp} & F_{ss} \end{pmatrix}\begin{pmatrix} E_p^i \\ E_s^i \end{pmatrix},$$

for the reflexion amplitudes, and

$$
\begin{pmatrix} M_{pp} & -\eta M_{ps} \\ -\eta^{-1} M_{sp} & M_{ss} \end{pmatrix} \begin{pmatrix} E_p^t \\ E_s^t \end{pmatrix} = 2k_z^i \begin{pmatrix} \sqrt{\epsilon_1 \epsilon_2}\, E_p^i \\ E_s^i \end{pmatrix},
$$

for the transmission field amplitudes, where $\eta = \sqrt{\epsilon_2/\epsilon_1}/F(\theta_i)$, $F(\theta_i) = k_z^t/k_z^i = \sqrt{(\epsilon_2/\epsilon_1) - \sin^2 \theta_i}/\cos \theta_i$. We shall not write the matrix $M_{\mu\nu}$ nor the source matrix $F_{\mu\nu}$ for brevity. Comparison with Eq. (B1) allows the Fresnel amplitudes to be identified. We display the result for $r_{\mu\nu}$ only:

$$
r_{pp} = \frac{\left(\epsilon_2 k_z^i - \epsilon_1 k_z^t + 4\pi \frac{\sigma_{xx}}{\omega} k_z^i k_z^t\right)\left(k_z^i + k_z^t + \frac{4\pi}{c} k_0 \sigma_{yy}\right) - \left(\frac{4\pi}{c}\right)^2 \sigma_{xy}\sigma_{yx} k_z^i k_z^t}{\left(\epsilon_2 k_z^i + \epsilon_1 k_z^t + 4\pi \frac{\sigma_{xx}}{\omega} k_z^i k_z^t\right)\left(k_z^i + k_z^t + \frac{4\pi}{c} k_0 \sigma_{yy}\right) - \left(\frac{4\pi}{c}\right)^2 \sigma_{xy}\sigma_{yx} k_z^i k_z^t}, \tag{B2}
$$

$$
r_{sp} = -\frac{\frac{8\pi}{c}\sigma_{yx}\sqrt{\epsilon_1}\, k_z^i k_z^t}{\left(\epsilon_2 k_z^i + \epsilon_1 k_z^t + 4\pi \frac{\sigma_{xx}}{\omega} k_z^i k_z^t\right)\left(k_z^i + k_z^t + \frac{4\pi}{c} k_0 \sigma_{yy}\right) - \left(\frac{4\pi}{c}\right)^2 \sigma_{xy}\sigma_{yx} k_z^i k_z^t}, \tag{B3}
$$

$$
r_{ps} = \frac{\frac{8\pi}{c}\sigma_{xy}\sqrt{\epsilon_1}\, k_z^i k_z^t}{\left(\epsilon_2 k_z^i + \epsilon_1 k_z^t + 4\pi \frac{\sigma_{xx}}{\omega} k_z^i k_z^t\right)\left(k_z^i + k_z^t + \frac{4\pi}{c} k_0 \sigma_{yy}\right) - \left(\frac{4\pi}{c}\right)^2 \sigma_{xy}\sigma_{yx} k_z^i k_z^t}, \tag{B4}
$$

$$
r_{ss} = \frac{\left(\epsilon_2 k_z^i + \epsilon_1 k_z^t + 4\pi \frac{\sigma_{xx}}{\omega} k_z^i k_z^t\right)\left(k_z^i - k_z^t - \frac{4\pi}{c} k_0 \sigma_{yy}\right) + \left(\frac{4\pi}{c}\right)^2 \sigma_{xy}\sigma_{yx} k_z^i k_z^t}{\left(\epsilon_2 k_z^i + \epsilon_1 k_z^t + 4\pi \frac{\sigma_{xx}}{\omega} k_z^i k_z^t\right)\left(k_z^i + k_z^t + \frac{4\pi}{c} k_0 \sigma_{yy}\right) - \left(\frac{4\pi}{c}\right)^2 \sigma_{xy}\sigma_{yx} k_z^i k_z^t}. \tag{B5}
$$

We can see that if $\sigma_{yx} = -\sigma_{xy}$, then $r_{sp} = r_{ps}$. Note also that if $|\sigma_{xy}\sigma_{yx}|/c^2 \ll 1$, then r_{pp} (r_{ss}) involves only the component σ_{xx} (σ_{yy}). For example, at normal incidence and for a free standing sample $T(\omega) \approx |t_{\mu\mu}|^2 \approx 1 - (4\pi/c)\text{Re}[\sigma_{ii}(\omega)]$, with $i = x$ for $\mu = p$ and $i = y$ for $\mu = s$, where $|\sigma_{ii}(\omega)|/c \ll 1$ is assumed for high enough frequencies in the range of interband transitions.

[1] V. Sih, R. Myers, Y. Kato, W. Lau, A. Gossard, and D. Awschalom, Spatial imaging of the spin Hall effect and current-induced polarization in two-dimensional electron gases, Nat. Phys. **1**, 31 (2005).

[2] R. R. Nair, P. Blake, A. N. Grigorenko, K. S. Novoselov, T. J. Booth, T. Stauber, N. M. Peres, and A. K. Geim, Fine structure constant defines visual transparency of graphene, Science **320**, 1308 (2008).

[3] L. Wu, M. Salehi, N. Koirala, J. Moon, S. Oh, and N. Armitage, Quantized Faraday and Kerr rotation and axion electrodynamics of a 3D topological insulator, Science **354**, 1124 (2016).

[4] A. Shuvaev, V. Dziom, Z. D. Kvon, N. N. Mikhailov, and A. Pimenov, Universal Faraday Rotation in HgTe Wells with Critical Thickness, Phys. Rev. Lett. **117**, 117401 (2016).

[5] L. M. Zhang, Z. Q. Li, D. N. Basov, M. M. Fogler, Z. Hao, and M. C. Martin, Determination of the electronic structure of bilayer graphene from infrared spectroscopy, Phys. Rev. B **78**, 235408 (2008).

[6] A. B. Kuzmenko, I. Crassee, D. van der Marel, P. Blake, and K. S. Novoselov, Determination of the gate-tunable band gap and tight-binding parameters in bilayer graphene using infrared spectroscopy, Phys. Rev. B **80**, 165406 (2009).

[7] R. Nandkishore and L. Levitov, Polar Kerr Effect and Time Reversal Symmetry Breaking in Bilayer Graphene, Phys. Rev. Lett. **107**, 097402 (2011).

[8] M. Offidani and A. Ferreira, Anomalous Hall Effect in 2D Dirac Materials, Phys. Rev. Lett. **121**, 126802 (2018).

[9] A. Dyrdał and J. Barnaś, Anomalous, spin, and valley Hall effects in graphene deposited on ferromagnetic substrates, 2D Materials **4**, 034003 (2017).

[10] G. Széchenyi, M. Vigh, A. Kormányos, and J. Cserti, Transfer matrix approach for the Kerr and Faraday rotation in layered nanostructures, J. Phys.: Condens. Matter **28**, 375802 (2016).

[11] I. Crassee, J. Levallois, A. L. Walter, M. Ostler, A. Bostwick, E. Rotenberg, T. Seyller, D. Van Der Marel, and A. B. Kuzmenko, Giant Faraday rotation in single and multilayer graphene, Nat. Phys. **7**, 48 (2011).

[12] W.-K. Tse and A. H. MacDonald, Giant Magneto-Optical Kerr Effect and Universal Faraday Effect in Thin-Film Topological Insulators, Phys. Rev. Lett. **105**, 057401 (2010).

[13] T. Wehling, A. M. Black-Schaffer, and A. V. Balatsky, Dirac materials, Adv. Phys. **63**, 1 (2014).

[14] J. Wang, S. Deng, Z. Liu, and Z. Liu, The rare two-dimensional materials with Dirac cones, Natl. Sci. Rev. **2**, 22 (2015).

[15] X.-F. Zhou, X. Dong, A. R. Oganov, Q. Zhu, Y. Tian, and H.-T. Wang, Semimetallic Two-Dimensional Boron Allotrope with Massless Dirac Fermions, Phys. Rev. Lett. **112**, 085502 (2014).

[16] A. Lopez-Bezanilla and P. B. Littlewood, Electronic properties of 8-*Pmmn* borophene, Phys. Rev. B **93**, 241405(R) (2016).

[17] L.-C. Xu, A. Du, and L. Kou, Hydrogenated borophene as a stable two-dimensional Dirac material with an ultrahigh Fermi velocity, Phys. Chem. Chem. Phys. **18**, 27284 (2016).

[18] M. Nakhaee, S. Ketabi, and F. Peeters, Tight-binding model for borophene and borophane, Phys. Rev. B **97**, 125424 (2018).

[19] M. Goerbig, J.-N. Fuchs, G. Montambaux, and F. Piéchon, Tilted anisotropic Dirac cones in quinoid-type graphene and α-(BEDT-TTF)$_2$I$_3$, Phys. Rev. B **78**, 045415 (2008).

[20] K. Kajita, Massless Dirac fermions realized in an organic crystal α-(BEDT-TTF)$_2$I$_3$, JPSJ News Comments **3**, 05 (2006).

[21] A. Kobayashi, S. Katayama, Y. Suzumura, and H. Fukuyama, Massless fermions in organic conductor, J. Phys. Soc. Jpn. **76**, 034711 (2007).

[22] T. Osada and A. Kiswandhi, Possible current-induced phenomena and domain control in an organic Dirac fermion system with weak charge ordering, J. Phys. Soc. Jpn. **89**, 103701 (2020).

[23] K. Yoshimura, M. Sato, and T. Osada, Experimental confirmation of massive Dirac fermions in weak charge-ordering state in α-(BEDT-TTF)$_2$I$_3$, J. Phys. Soc. Jpn. **90**, 033701 (2021).

[24] X. Qian, J. Liu, L. Fu, and J. Li, Quantum spin Hall effect in two-dimensional transition metal dichalcogenides, Science **346**, 1344 (2014).

[25] C.-Y. Tan, C.-X. Yan, Y.-H. Zhao, H. Guo, and H.-R. Chang, Anisotropic longitudinal optical conductivities of tilted Dirac bands in $1T'$-MoS$_2$, Phys. Rev. B **103**, 125425 (2021).

[26] H.-Y. Lu, A. S. Cuamba, S.-Y. Lin, L. Hao, R. Wang, H. Li, Y. Zhao, and C. S. Ting, Tilted anisotropic Dirac cones in partially hydrogenated graphene, Phys. Rev. B **94**, 195423 (2016).

[27] Z.-K. Yang, J.-R. Wang, and G.-Z. Liu, Effects of Dirac cone tilt in a two-dimensional Dirac semimetal, Phys. Rev. B **98**, 195123 (2018).

[28] K. Sadhukhan and A. Agarwal, Anisotropic plasmons, Friedel oscillations, and screening in 8-*Pmmn* borophene, Phys. Rev. B **96**, 035410 (2017).

[29] J. Sári, C. Tőke, and M. O. Goerbig, Magnetoplasmons of the tilted anisotropic Dirac cone material α-(BEDT-TTF)$_2$I$_3$, Phys. Rev. B **90**, 155446 (2014).

[30] S. F. Islam and A. M. Jayannavar, Signature of tilted Dirac cones in Weiss oscillations of 8-*Pmmn* borophene, Phys. Rev. B **96**, 235405 (2017).

[31] S. Rostamzadeh, I. Adagideli, and M. O. Goerbig, Large enhancement of conductivity in Weyl semimetals with tilted cones: Pseudorelativity and linear response, Phys. Rev. B **100**, 075438 (2019).

[32] S. Verma, A. Mawrie, and T. K. Ghosh, Effect of electron-hole asymmetry on optical conductivity in 8-*Pmmn* borophene, Phys. Rev. B **96**, 155418 (2017).

[33] Y. Suzumura, I. Proskurin, and M. Ogata, Effect of tilting on the in-plane conductivity of Dirac electrons in organic conductor, J. Phys. Soc. Jpn. **83**, 023701 (2014).

[34] Y. Suzumura, I. Proskurin, and M. Ogata, Dynamical conductivity of Dirac electrons in organic conductors, J. Phys. Soc. Jpn. **83**, 094705 (2014).

[35] K. Kristinsson, O. V. Kibis, S. Morina, and I. A. Shelykh, Control of electronic transport in graphene by electromagnetic dressing, Sci. Rep. **6**, 20082 (2016).

[36] T. Oka and H. Aoki, Photovoltaic Hall effect in graphene, Phys. Rev. B **79**, 081406(R) (2009).

[37] S. Syzranov, M. Fistul, and K. Efetov, Effect of radiation on transport in graphene, Phys. Rev. B **78**, 045407 (2008).

[38] H. L. Calvo, H. M. Pastawski, S. Roche, and L. E. F. Torres, Tuning laser-induced band gaps in graphene, Appl. Phys. Lett. **98**, 232103 (2011).

[39] A. E. Champo and G. G. Naumis, Metal-insulator transition in 8-*Pmmn* borophene under normal incidence of electromagnetic radiation, Phys. Rev. B **99**, 035415 (2019).

[40] V. Ibarra-Sierra, J. Sandoval-Santana, A. Kunold, and G. G. Naumis, Dynamical band gap tuning in anisotropic tilted Dirac semimetals by intense elliptically polarized normal illumination and its application to 8-*Pmmn* borophene, Phys. Rev. B **100**, 125302 (2019).

[41] J. Yuan, N. Yu, K. Xue, and X. Miao, Ideal strength and elastic instability in single-layer 8-*Pmmn* borophene, RSC Advances **7**, 8654 (2017).

[42] J. Sandoval-Santana, V. Ibarra-Sierra, A. Kunold, and G. G. Naumis, Floquet spectrum for anisotropic and tilted Dirac materials under linearly polarized light at all field intensities, J. Appl. Phys. **127**, 234301 (2020).

[43] K. Komatsu, Y. Morita, E. Watanabe, D. Tsuya, K. Watanabe, T. Taniguchi, and S. Moriyama, Observation of the quantum valley Hall state in ballistic graphene superlattices, Sci. Adv. **4**, eaaq0194 (2018).

[44] K. S. Novoselov, E. McCann, S. Morozov, V. I. Fal'ko, M. Katsnelson, U. Zeitler, D. Jiang, F. Schedin, and A. Geim, Unconventional quantum Hall effect and Berry's phase of 2π in bilayer graphene, Nat. Phys. **2**, 177 (2006).

[45] F. D. M. Haldane, Model for a Quantum Hall Effect without Landau Levels: Condensed-Matter Realization of the "Parity Anomaly," Phys. Rev. Lett. **61**, 2015 (1988).

[46] A. Hill, A. Sinner, and K. Ziegler, Valley symmetry breaking and gap tuning in graphene by spin doping, New J. Phys. **13**, 035023 (2011).

[47] B. R. Matis, B. H. Houston, and J. W. Baldwin, Evidence for spin glass ordering near the weak to strong localization transition in hydrogenated graphene, ACS Nano **10**, 4857 (2016).

[48] L. Stille, C. J. Tabert, and E. J. Nicol, Optical signatures of the tunable band gap and valley-spin coupling in silicene, Phys. Rev. B **86**, 195405 (2012).

[49] T. Osada, Chern insulator phase in a lattice of an organic Dirac semimetal with intracellular potential and magnetic modulations, J. Phys. Soc. Jpn. **86**, 123702 (2017).

[50] M. Vila, N. T. Hung, S. Roche, and R. Saito, Tunable circular dichroism and valley polarization in the modified Haldane model, Phys. Rev. B **99**, 161404(R) (2019).

[51] T. Nishine, A. Kobayashi, and Y. Suzumura, Tilted-cone induced cusps and nonmonotonic structures in dynamical polarization function of massless Dirac fermions, J. Phys. Soc. Jpn. **79**, 114715 (2010).

[52] A. Singh, S. Ghosh, and A. Agarwal, Nonlinear and anisotropic polarization rotation in two-dimensional Dirac materials, Phys. Rev. B **97**, 205420 (2018).

[53] A. Zabolotskiy and Y. E. Lozovik, Strain-induced pseudomagnetic field in the Dirac semimetal borophene, Phys. Rev. B **94**, 165403 (2016).

[54] T. Farajollahpour, Z. Faraei, and S. A. Jafari, Solid-state platform for space-time engineering: The 8-*Pmmn* borophene sheet, Phys. Rev. B **99**, 235150 (2019).

[55] Z. Zhang, E. S. Penev, and B. I. Yakobson, Two-dimensional boron: Structures, properties, and applications, Chem. Soc. Rev. **46**, 6746 (2017).

[56] S.-H. Zhang and W. Yang, Oblique Klein tunneling in 8-*Pmmn* borophene *p-n* junctions, Phys. Rev. B **97**, 235440 (2018).

[57] Z. Jalali-Mola and S. A. Jafari, Polarization tensor for tilted Dirac fermion materials: Covariance in deformed Minkowski spacetime, Phys. Rev. B **100**, 075113 (2019).

[58] S.-G. Xu, X.-T. Li, Y.-J. Zhao, W.-P. Xu, J.-H. Liao, X.-W. Zhang, H. Xu, and X.-B. Yang, Insights into the unusual semi-conducting behavior in low-dimensional boron, Nanoscale **11**, 7866 (2019).

[59] D. V. P. Massote, L. Liang, N. Kharche, and V. Meunier, Electronic, vibrational, Raman, and scanning tunneling microscopy signatures of two-dimensional boron nanomaterials, Phys. Rev. B **94**, 195416 (2016).

[60] P. Sengupta, Y. Tan, E. Bellotti, and J. Shi, Anomalous heat flow in 8-*Pmmn* borophene with tilted Dirac cones, J. Phys.: Condens. Matter **30**, 435701 (2018).

[61] X. Zhou, Anomalous Andreev reflection in an 8-*Pmmn* borophene-based superconducting junction, Phys. Rev. B **102**, 045132 (2020).

[62] Z.-Q. Wang, T.-Y. Lü, H.-Q. Wang, Y. P. Feng, and J.-C. Zheng, Band gap opening in 8-*Pmmn* borophene by hydrogenation, ACS Appl. Electron. Mater. **1**, 667 (2019).

[63] S.-Y. Xu, Q. Ma, H. Shen, V. Fatemi, S. Wu, T.-R. Chang, G. Chang, A. M. M. Valdivia, C.-K. Chan, Q. D. Gibson *et al.*, Electrically switchable Berry curvature dipole in the monolayer topological insulator WTe$_2$, Nat. Phys. **14**, 900 (2018).

[64] G. Jotzu, M. Messer, R. Desbuquois, M. Lebrat, T. Uehlinger, D. Greif, and T. Esslinger, Experimental realization of the topological Haldane model with ultracold fermions, Nature **515**, 237 (2014).

[65] P. Kapri, B. Dey, and T. K. Ghosh, Valley caloritronics in a photodriven heterojunction of Dirac materials, Phys. Rev. B **102**, 045417 (2020).

[66] P. Sengupta and E. Bellotti, Anomalous Lorenz number in massive and tilted Dirac systems, Appl. Phys. Lett. **117**, 223103 (2020).

[67] H. Rostami and V. Juričić, Probing quantum criticality using nonlinear Hall effect in a metallic Dirac system, Phys. Rev. Research **2**, 013069 (2020).

[68] V. P. Gusynin, S. G. Sharapov, and J. P. Carbotte, Unusual microwave Response of Dirac Quasiparticles in Graphene, Phys. Rev. Lett. **96**, 256802 (2006).

[69] T. Stauber, P. San-Jose, and L. Brey, Optical conductivity, Drude weight, and plasmons in twisted graphene bilayers, New J. Phys. **15**, 113050 (2013).

[70] K. Ghalamkari, Y. Tatsumi, and R. Saito, Perfect circular dichroism in the Haldane model, J. Phys. Soc. Jpn. **87**, 063708 (2018).